



Mechanical force application to the nucleus regulates nucleocytoplasmic transport

Ion Andreu^{1,2,10}✉, Ignasi Granero-Moya^{1,3,10}, Nimesh R. Chahare¹, Kesseem Clein⁴, Marc Molina-Jordán^{1,3}, Amy E. M. Beedle^{1,5}, Alberto Elosegui-Artola^{1,5,6,7}, Juan F. Abenza¹, Leone Rossetti¹, Xavier Trepot^{1,3,8,9}, Barak Raveh⁴ and Pere Roca-Cusachs^{1,3}✉

Mechanical force controls fundamental cellular processes in health and disease, and increasing evidence shows that the nucleus both experiences and senses applied forces. Such forces can lead to the nuclear translocation of proteins, but whether force controls nucleocytoplasmic transport, and how, remains unknown. Here we show that nuclear forces differentially control passive and facilitated nucleocytoplasmic transport, setting the rules for the mechanosensitivity of shuttling proteins. We demonstrate that nuclear force increases permeability across nuclear pore complexes, with a dependence on molecular weight that is stronger for passive than for facilitated diffusion. Owing to this differential effect, force leads to the translocation of cargoes into or out of the nucleus within a given range of molecular weight and affinity for nuclear transport receptors. Further, we show that the mechanosensitivity of several transcriptional regulators can be both explained by this mechanism and engineered exogenously by introducing appropriate nuclear localization signals. Our work unveils a mechanism of mechanically induced signalling, probably operating in parallel with others, with potential applicability across signalling pathways.

Cells sense and respond to mechanical stimuli from their environment by a process known as mechanosensing, which drives important processes in health and disease^{1–3}. Growing evidence shows that the cell nucleus is directly submitted to force^{4–6}, and can act as a mechanosensor⁷. Force applied to the nucleus (henceforth termed nuclear force for simplicity) can affect chromatin architecture⁸, the accessibility of the transcription machinery⁹, the conformation of nucleoskeletal proteins such as lamins¹⁰, or cell contractility^{11,12}. Further, forces transmitted to cells, and specifically nuclei, affect the nucleocytoplasmic localization of transcriptional regulators involved in different signalling pathways¹³. As proposed for MRTF-A^{14,15}, β-catenin^{16,17} or YAP^{18–20}, this can be due to a retention mechanism in which force controls the localization of proteins by regulating their affinity for binding partners in the nucleus or cytoplasm. Alternatively, the nuclear translocation of YAP⁶ and MyoD²¹ has been associated with a force-induced increase in passive diffusion across nuclear pore complexes (NPCs). From this evidence, it is tempting to hypothesize that nucleocytoplasmic transport could be mechanosensitive per se, independently of any specific signalling pathway. This would enable a general mechanism by which nuclear force could control the nuclear localization of proteins, and thereby transcription. However, mere changes in passive diffusion can provide neither directionality nor molecular specificity, so whether there is such a mechanism, and how it operates, remains unknown.

Nucleocytoplasmic transport takes place through NPCs in two main ways: passive and facilitated diffusion^{22,23}. Passive diffusion is rapid for small proteins, but is progressively impaired as the molecular

weight (MW) of the protein increases^{24–26}. This impairment is caused by a meshwork of disordered proteins within NPCs called phenylalanine–glycine nucleoporins (FG Nups), commonly termed the NPC permeability barrier²⁷. Facilitated diffusion of larger proteins is mediated by nuclear transport receptors^{28,29}, which interact specifically with both the cargo molecules and FG Nups to overcome the NPC permeability barrier. They are divided between importins (mediating active nuclear import) and exportins (mediating active nuclear export)³⁰. Both classes interact with cargoes by binding to specific sequences³¹ termed nuclear localization signals (NLS) or nuclear export signals (NES) for proteins binding to importins or exportins, respectively^{32,33}. The directionality of facilitated transport in either the import or export direction is enabled by the coupling of binding/unbinding events to the phosphorylation status of the small GTPase Ran (either GTP, predominant in the nucleus, or GDP, predominant in the cytoplasm)²⁹. For example, in canonical import, a complex is formed between importin β (which interacts with FG Nups), importin α (which binds importin β) and the cargo (which binds importin α through an NLS). The complex then diffuses through the NPC and finally dissociates in the nucleus in a RanGTP-dependent manner^{30,31}. In this article, we study how nuclear force regulates both passive and facilitated diffusion, and how this can provide mechanosensitivity to the nuclear localization of shuttling proteins.

Results

Nucleocytoplasmic transport is mechanosensitive. To assess if and how mechanical force affects nucleocytoplasmic transport, we studied different artificial constructs undergoing both passive and

¹Institute for Bioengineering of Catalonia (IBEC), the Barcelona Institute of Technology (BIST), Barcelona, Spain. ²Universidad de Navarra, TECNUN Escuela de Ingeniería, Donostia-San Sebastián, Spain. ³Universitat de Barcelona, Barcelona, Spain. ⁴School of Computer Science and Engineering, The Hebrew University of Jerusalem, Jerusalem, Israel. ⁵Department of Physics, King's College London, London, UK. ⁶Harvard John A. Paulson School of Engineering and Applied Sciences, Harvard University, Cambridge, MA, USA. ⁷Cell and Tissue Mechanobiology Laboratory, The Francis Crick Institute, London, UK. ⁸Institució Catalana de Recerca i Estudis Avançats (ICREA), Barcelona, Spain. ⁹Centro de Investigación Biomédica en Red en Bioningeniería, Biomateriales y Nanomedicina (CIBER-BBN), Barcelona, Spain. ¹⁰These authors contributed equally: Ion Andreu, Ignasi Granero-Moya. ✉e-mail: iandreu@ibecbarcelona.eu; proca@ibecbarcelona.eu

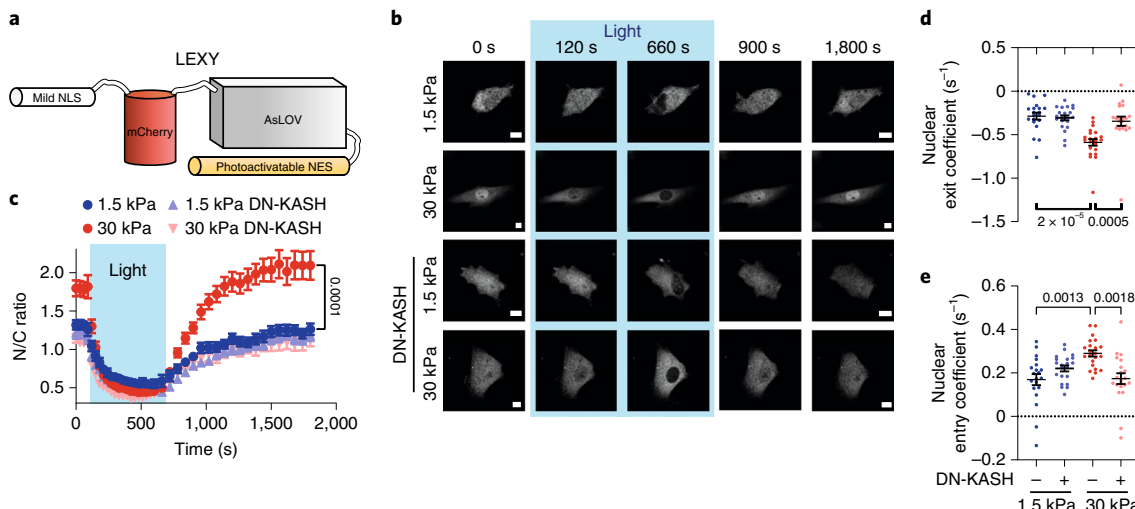


Fig. 1 | Nucleocytoplasmic transport is mechanosensitive. **a**, Cartoon of light-activated nucleocytoplastic shuttling construct. Mild NLS is always active, NES is activated only upon light excitation of LOV2 domain from *Avena sativa* phototropin1 (AsLOV). **b**, Time sequences of construct fluorescence before, during and after excitation for cells seeded on 1.5/30 kPa substrates, with or without DN-KASH overexpression. Scale bars, 20 μ m. **c-e**, Corresponding quantifications of N/C ratios, and coefficients of exit and subsequent re-entry of constructs into the nucleus (in units of s^{-1} , obtained by fitting an exponential to the curves, see Methods). $N=20, 22, 21$ and 21 cells per condition 1.5 kPa, 30 kPa, 1.5 kPa DN-KASH and 30 kPa DN-KASH, respectively, from three independent experiments; data are presented as mean \pm standard error of the mean (s.e.m.). In **c**, the bar indicates the statistical significance between the last timepoint of 1.5 kPa and 30 kPa values. In **d** and **e**, P values were calculated with two-way ANOVA Šídák's multiple comparisons test. Source numerical data are available in source data.

facilitated diffusion, transfected in mouse embryonic fibroblasts. First, we used a light-inducible nuclear export construct (LEXY)³⁴ (Fig. 1a). The construct presents a mild NLS fused to mCherry, plus a stronger NES that is only functional upon light excitation. To control the mechanical environment, cells were seeded on soft or stiff fibronectin-coated polyacrylamide gels (Young's modulus of 1.5 and 30 kPa, respectively). Increasing substrate stiffness leads to the growth of focal adhesions, increasing the transmission of actomyosin-generated forces between cells and the substrate^{35,36}. In turn, these forces reach and deform the nucleus through the linker of nucleus and cytoskeleton (LINC) complex^{4,6}, which connects actin fibres to the nuclear lamina. Before photoactivation ($t=0$), with only the NLS active, the nuclear-to-cytoplasmic ratio (N/C ratio) was higher for cells on stiff substrates (Fig. 1b,c). Upon excitation by light, the construct exited the nucleus to similar final N/C ratios in both conditions, although the rate of N/C change was higher for the stiff substrate (Fig. 1b-d). Once light excitation stopped, the reverse process occurred, with N/C ratios increasing faster for the stiff substrate, until restoring original values (Fig. 1e). We then co-transfected cells with dominant negative (DN)-KASH, a dominant-negative domain of nesprin that disrupts the LINC complex⁴ and prevents force transmission to the nucleus⁶. DN-KASH overexpression led cells on stiff substrates to behave like those on soft substrates (Fig. 1b-e), demonstrating that the effect of stiffness was mediated by nuclear force.

Passive diffusion is mechanosensitive for small MWs. Our results strongly suggest that nucleocytoplastic transport is generally affected by nuclear force, but do not clarify the contributions of passive and facilitated diffusion (the ~45 kDa LEXY construct is probably sufficiently small to diffuse passively). To dissect the different contributions, we first used constructs undergoing only passive diffusion, and regulated their diffusivity through their MW. These constructs were composed of a green fluorescent protein (GFP), attached through a short linker to between zero and six repeats of the 7 kDa bacterial protein A (PrA) (Fig. 2a). PrA is inert and purely

diffusive in eukaryotic cells, as shown previously²⁵ and also confirmed by the complete fluorescence recovery of the constructs after photobleaching (Extended Data Fig. 1e). When we transfected the constructs in cells, the N/C ratios of all proteins were ~1 regardless of MW and substrate stiffness (Fig. 2b,c).

This result shows that concentrations of passively diffusing proteins were not mechanosensitive (where mechanosensitivity is defined as the fold change in a given magnitude in stiff versus soft substrates). However, this does not provide information on diffusion kinetics. To quantify this, we adapted a previously described method and model²⁰ based on fluorescence loss in photobleaching (FLIP; Fig. 2d), which allowed us to measure nuclear influx and efflux rates (Methods and Extended Data Fig. 1). These rates quantify overall transport into and out of the nucleus, regardless of whether it is passive or mediated by active import or export. As expected, both influx and efflux rates decreased with MW (Fig. 2e,f). Interestingly, rates increased with substrate stiffness, and this effect decreased for increasing MW (Fig. 2e,f). Confirming that this was mediated by nuclear force, DN-KASH overexpression had the same effect as reducing substrate stiffness (Extended Data Fig. 2). Thus, nuclear force weakens the permeability barrier of NPCs (that is, increases diffusion), and the effect is more pronounced for molecules with low MW (high diffusivity). Nevertheless, and because diffusion is non-directional, this does not affect the steady-state nucleocytoplastic distribution of molecules, which remains uniform.

Mechanosensitivity of facilitated versus passive diffusion. Next, we assessed how substrate stiffness affected facilitated transport. We first assessed the protein directly interacting with FG Nups, importin β . As expected, transfected importin β -GFP localized at the nuclear membrane (Fig. 3a). Owing to this localization and the diffraction limit, our FLIP measurements could not capture the probably very fast kinetics taking place in the immediate vicinity of the nuclear membrane. However, we did measure the kinetics of importin β molecules released in the bulk of either the nucleus or cytoplasm. Influx and efflux rates of importin β showed a high

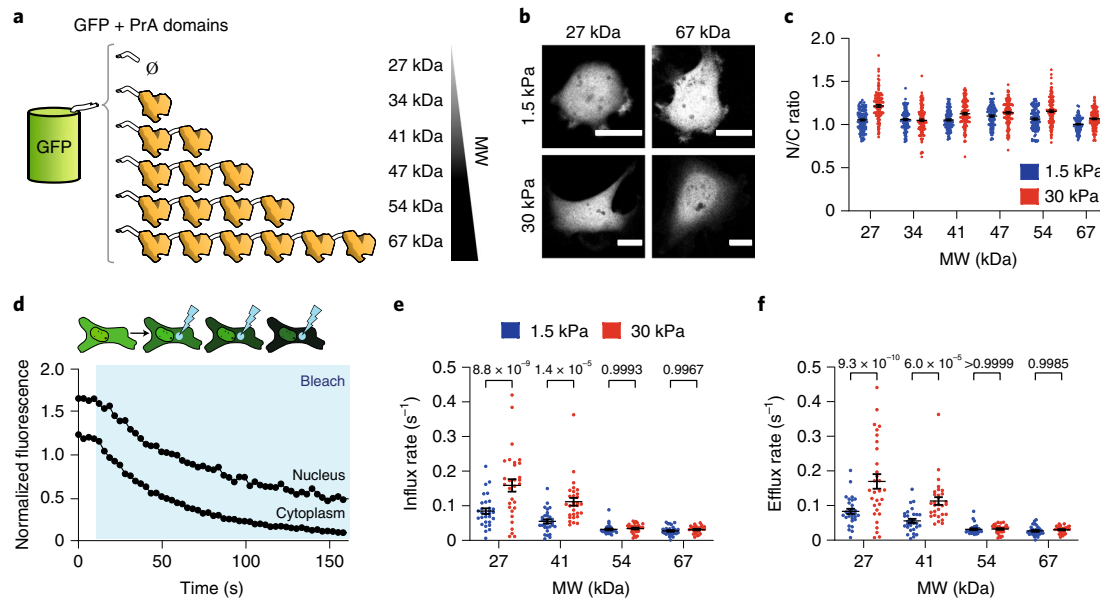


Fig. 2 | Passive diffusion through NPCs is mechanosensitive for small MWs. **a**, Cartoon of constructs with EGFP and different amount of repeats of PrA domains. **b**, Images showing fluorescence of indicated constructs on 1.5 kPa or 30 kPa substrates. **c**, N/C ratios of constructs on 1.5 kPa or 30 kPa substrates as a function of MW. $N=120$ cells from three independent experiments. Significant effects of stiffness and MW were observed ($P<1\times 10^{-15}$ and $P<1\times 10^{-15}$, respectively; computed via two-way ANOVA). **d**, Example of a FLIP experiment: a laser photobleaches a region of the cell cytoplasm, and fluorescence intensities are recorded over time in nucleus and cytoplasm. Resulting curves are fitted to a kinetic model to obtain influx and efflux rates (see Methods). **e,f**, Influx and efflux rates on 1.5 kPa and 30 kPa substrates as a function of MW of the constructs. $N=30$ cells from three independent experiments. The effects of substrate stiffness and MW were significant in both **e** ($P=2.9\times 10^{-8}$ and $P<1\times 10^{-15}$, respectively) and **f** ($P=4.0\times 10^{-8}$ and $P<1\times 10^{-15}$, respectively), computed via two-way ANOVA. Scale bars, 20 μ m. Data are mean \pm s.e.m. Source numerical data are available in source data.

mechanosensitivity (Fig. 3b,c), similarly to that of highly diffusive passive molecules (Fig. 2e,f). As importin β exhibits facilitated diffusion both in the influx and efflux direction, influx and efflux rates were largely symmetrical, leading to uniform concentrations inside and outside the nucleus regardless of substrate stiffness (Fig. 3d).

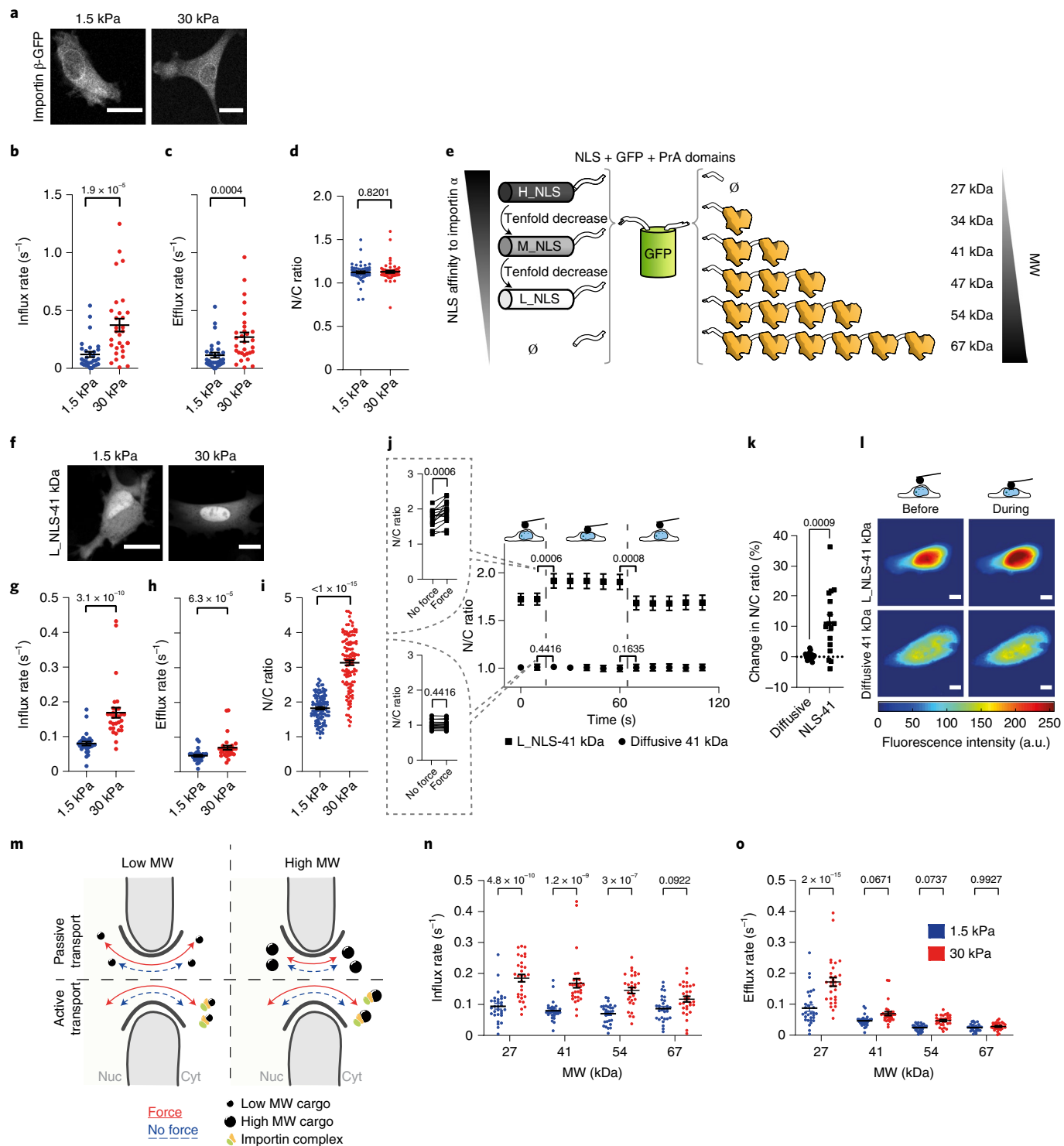
Then, we studied cargo proteins undergoing facilitated diffusion by adding NLS sequences to the GFP-PrA constructs (Fig. 3e). To regulate facilitated diffusion, we used NLS sequences with point mutations resulting in varying levels of affinity for importin α (ref. ³⁷). We termed them H_NLS, M_NLS and L_NLS, for high, medium and low affinity, respectively (Supplementary Table 2). The mechanosensitivity of such constructs can be predicted from the behaviour of passively diffusing molecules (Fig. 2e,f) and importin β (Fig. 3b,c). Indeed, a cargo molecule with an NLS should have a high mechanosensitivity in the influx direction (because it enters the nucleus with importin β), but a low mechanosensitivity in the efflux direction if its MW is above ~ 40 kDa (because it exits the nucleus through passive diffusion, which loses mechanosensitivity as MW increases).

By taking L_NLS-EGFP-2PrA (41 kDa) as a starting point, we confirmed this prediction: this molecule had higher mechanosensitivity in influx than efflux rates, leading to an increase in N/C ratios with stiffness (Fig. 3f-i). We then carried out several controls to confirm that this was caused by nuclear force. First, we checked that the same effects on rates were observed when comparing cells with and without DN-KASH overexpression (Extended Data Fig. 2). Second, we assessed stiffness-mediated changes in importin concentrations. Concentrations of importin β did not change with stiffness, but the two types of importin α binding to our NLS constructs (importin $\alpha 3$ and importin $\alpha 1$) respectively showed a $\sim 50\%$ increase or $\sim 40\%$ decrease with stiffness (Extended Data Fig. 3a-e). The N/C ratios of importins remained close to 1 in all cases, with only a $\sim 10\text{--}30\%$ increase with stiffness that, if anything, should impair, rather than

promote, nuclear import of cargo (Extended Data Fig. 3). Thus, changes in importin concentration may have an impact, but do not exhibit any consistent trend that could explain our results. Finally, we applied force to the nucleus of cells seeded on soft gels with atomic force microscopy (AFM), and verified that this also led to an increase in N/C ratios only if the construct contained the L_NLS sequence (Fig. 3j-l). Applying force to cells co-transfected with L_NLS-EGFP-2PrA and purely diffusive BFP also led to a nuclear enrichment of GFP versus BFP (Extended Data Fig. 3). Response to AFM-applied force was also lost for cells overexpressing DN-KASH, showing that the effects of force require an intact LINC complex (Extended Data Fig. 3).

For L_NLS-EGFP-2PrA, nuclear accumulation with force is explained by a higher mechanosensitivity of facilitated versus passive diffusion. This differential behaviour may arise from the role of MW. Indeed, passive diffusion is strongly impaired as MW increases²⁵, whereas facilitated diffusion can transport large molecules³⁸⁻⁴⁰. Thus, one could expect a scheme (summarized in Fig. 3m) in which passive diffusion decreases both in magnitude and in mechanosensitivity as MW increases (as measured in Fig. 2e,f) whereas facilitated transport is not affected (or only mildly affected) by MW. To verify this hypothesis, we measured influx and efflux rates of constructs containing the L_NLS sequence and different MW (Fig. 3n,o). Indeed, influx rates (dominated by active transport, Fig. 3m) had a much milder dependence on MW than efflux rates (dominated by diffusion and with very similar behaviour to that of purely diffusive constructs, Fig. 3o).

Molecular properties defining mechanosensitivity. With these elements, we can generate an initial conceptual model of how nucleocytoplasmic transport should broadly depend on force, MW and NLS affinity (Supplementary Note). To this end, we assume that N/C ratios are given by the ratio of influx and efflux rates, where



efflux rates are purely passive and influx rates have additive contributions of both passive and facilitated diffusion. Then, we assume as experimentally verified that (1) passive influx and efflux rates (which are equal) decrease as MW increases; (2) passive influx and efflux rates increase when nuclear force is applied, but this effect disappears as MW increases; (3) facilitated influx rates increase with nuclear force and with NLS sequence affinity, but do not depend on MW. We also assume that there is a limit to the efficiency of active facilitated transport, and therefore (4) N/C ratios saturate and cannot increase above a given level. In such a saturation regime, changes in influx and efflux rates can no longer behave differently

and should be matched. The potential origin of this is discussed in the more detailed, kinetic model introduced later in this paper. With these assumptions, we can plot two simple diagrams showing how N/C ratios should depend on MW and NLS affinity before applying force to the nucleus (Fig. 4a), and their fold change with force, that is, their mechanosensitivity (Fig. 4b). According to this framework, for low MW or a weak NLS, passive diffusion dominates over facilitated import, leading to N/C ratios close to 1 independently of nuclear force. For high MW or strong NLS, facilitated import dominates over diffusion, leading to high, saturated N/C ratios, also independently of nuclear force. However, when passive and facilitated

Fig. 3 | Differential mechanosensitivity of facilitated import versus passive diffusion explains force-induced nuclear translocation. **a**, Example importin β-GFP images for cells on 1.5 kPa and 30 kPa substrates. **b-d**, Corresponding importin β-GFP influx rates (**b**), efflux rates (**c**) and resulting N/C ratios (**d**). $N=30, 30$ and 60 cells from three independent experiments. P values were calculated with two-tailed Mann–Whitney test. **e**, Cartoon of constructs with EGFP, different number of repeats of PrA domains, and NLS of different affinities to importin α. **f**, Example images of L-NLS-41 kDa construct for cells on 1.5 kPa and 30 kPa substrates. **g-i**, Corresponding influx rates (**g**), efflux rates (**h**) and resulting N/C ratios (**i**) of L-NLS-41 kDa construct. $N=30, 30$ and 120 cells from three independent experiments, respectively. P values were calculated with two-tailed Mann–Whitney test. **j**, N/C ratios of L-NLS-41 kDa or diffusive 41 kDa constructs in cells seeded on 1.5 kPa gels before, during and after nuclear deformation with AFM. Graphs on the left show paired dot plots of the timepoints right before and after force application. P values were calculated with two-tailed paired *t*-test. **k**, Corresponding percentage change in N/C ratios right after force application for both constructs. P value was calculated with a two-tailed unpaired *t*-test with Welch's correction. In **j** and **k**, $N=16$ cells from three independent experiments; traces of all cells are shown in Extended Data Fig. 8. **l**, Corresponding images of constructs before and during force application; dotted line marks nucleus outline. Scale bars, 20 μm. **m**, Cartoon summarizing the effects of nuclear force and MW on active and passive transport. Passive transport decreases with MW, and depends on force only for low-MW molecules. Active transport does not depend on MW, and depends on force regardless of MW. Note that active transport arrows also show a small arrow in the export direction, as discussed in the text. **n**, Influx rates (mediated by facilitated transport) of L-NLS constructs with different MW. The effect of substrate stiffness and MW was $P<1\times 10^{-15}$ and $P=0.0004$, respectively. **o**, Efflux rates of L-NLS constructs (mediated by passive transport) with different MW. The effect of substrate stiffness and MW was $P=3.5\times 10^{-11}$ and $P<1\times 10^{-15}$, respectively. In **n** and **o**, $N=30$ cells from three independent experiments. Two-way ANOVA and Šídák's multiple comparisons test were used to obtain P values between conditions. Data are mean \pm s.e.m. in all panels. Source numerical data are available in source data.

rates are comparable, they depend differently on force, leading to mechanosensitive N/C ratios. As MW decreases (and passive diffusion increases), a progressively higher facilitated influx is required to match passive diffusion, and thus the ‘mechanosensitive zone’ is placed along a diagonal in Fig. 4b.

We then verified the different predictions of the conceptual model by using the different constructs. First, for proteins with a fixed NLS sequence (L-NLS), N/C ratios increased with MW monotonically, but mechanosensitivity peaked at an intermediate MW between the high passive diffusion regime (low MW) and the saturated regime (high MW) (Fig. 4c,f,i). Of note, increasing N/C ratios also led to increased variability in measurements, due to the increased noise caused by the low cytoplasmic signal (Extended Data Fig. 4). Second, increasing MW in proteins with a fixed NLS sequence of higher affinity (M-NLS) moved the point of maximum mechanosensitivity to a lower MW (Fig. 4d,g,j). Finally, increasing NLS affinity in proteins with a fixed MW (41 kDa) also increased N/C ratios monotonically, but affected mechanosensitivity in a biphasic manner (Fig. 4e,h,k). For this last set of constructs, we also used the highly nuclear and not mechanosensitive H-NLS construct to verify that force application with AFM did not lead to the same response as in mechanosensitive constructs (Extended Data Fig. 3).

Our conceptual model thus provides a useful framework to interpret our results, but it does not consider important elements of nucleocytoplastic transport, such as the Ran cycle, or the fact that facilitated transport is reversible and can operate in both directions⁴¹. To address this, we developed a more elaborate kinetic mathematical model that follows a canonical description of importin-mediated nucleocytoplastic transport. This includes docking, undocking and bidirectional translocation of importins in different intermediate forms, competitive binding of cargo and RanGTP to importins, the Ran cycle and passive diffusion of unbound cargo molecules (Supplementary Note)^{30,42–44}. To model the effect of force on passive

diffusion, we used the experimentally measured passive diffusion rates as a function of force and MW from Fig. 2e,f. For facilitated diffusion, we simply assumed that force reduces the mean time required for importin–cargo complexes to cross NPCs (in an MW-independent way), without changing any other parameter.

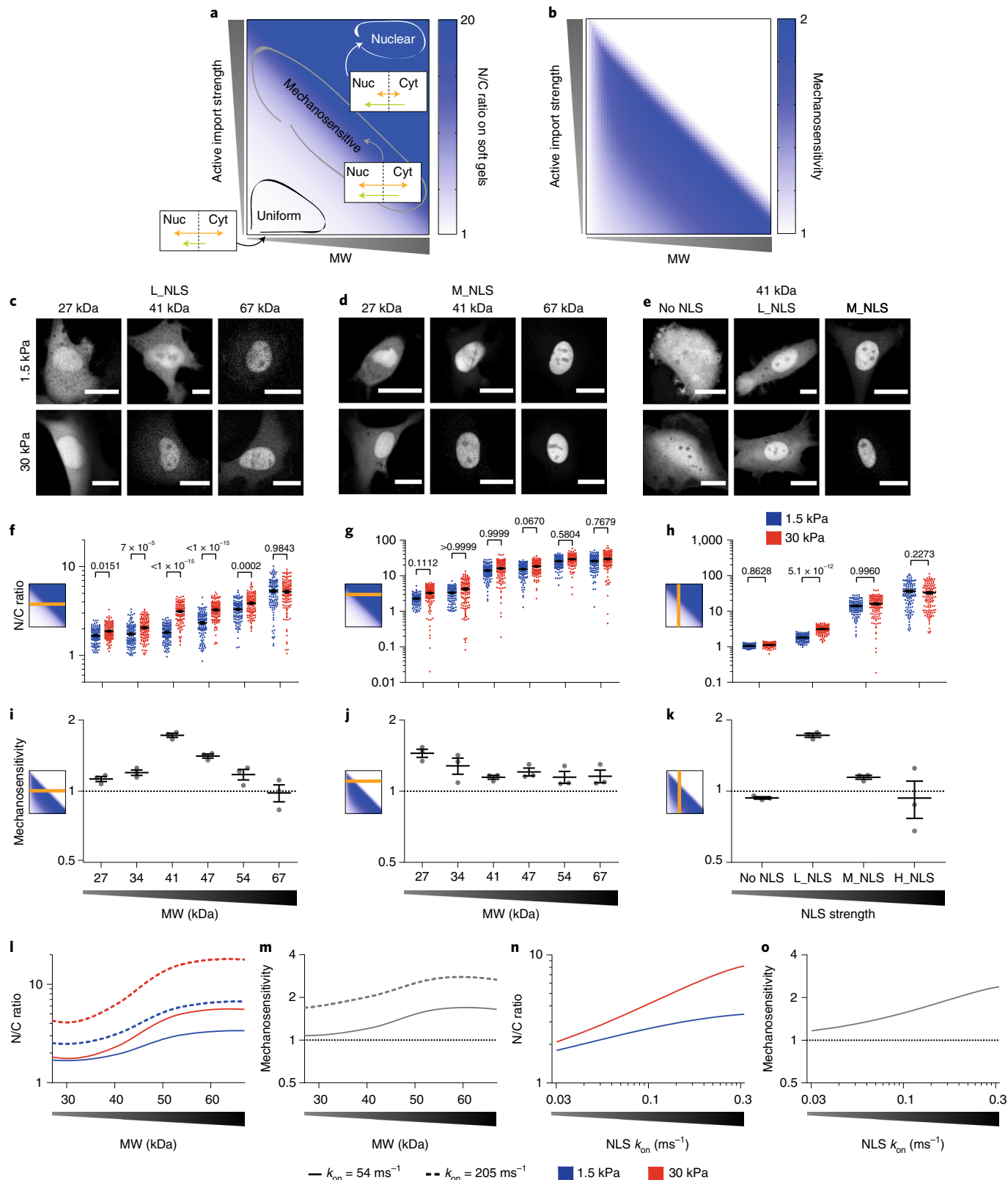
The kinetic model correctly predicted the increase of N/C ratios, and of their mechanosensitivity, with MW and NLS affinity (Fig. 4l–o). Interestingly, as NLS affinities increase, the model predicted an increase in not only influx rates but to a lesser degree also efflux rates, something which we confirmed experimentally (Extended Data Fig. 5). This occurs because, as NLS affinity increases, cargo molecules can compete with Ran-GTP for binding importins, limiting the ability of Ran-GTP to disassemble the cargo–importin complex. This leads to the facilitated diffusion of importin–cargo complexes out of (not only into) the nucleus. Eventually, for very high NLS affinities, the model predicted that N/C ratios would first saturate and then collapse, as cargo becomes so tightly bound to importins that it diffuses with it out of the nucleus regardless of Ran-GTP (Extended Data Fig. 5). This was not observed in experiments, and probably corresponds to non-physiological high affinities. The only experimental feature that the kinetic model did not capture was the fact that high MWs or NLS affinities decreased mechanosensitivity (Fig. 4i–k). Instead, the model predicted that mechanosensitivity should be maintained even in this regime (Fig. 4m,o). Potentially, this could be because the model underestimated the effect of NLS affinity on efflux rates (Extended Data Fig. 5). If efflux rates are mediated by facilitated rather than passive diffusion, then their dependency on force is the same as that of influx rates, and the overall effect on N/C ratios cancels out.

Mechanosensitivity of facilitated export. Given the observed mechanosensitivity of active nuclear import, one might expect a similar (but reversed) behaviour for active export. To test this, we

Fig. 4 | Balance between affinity to importins and MW defines the mechanosensitivity of nuclear localization. **a,b**, Qualitative prediction from conceptual model of how MW and affinity to importins should affect N/C ratios (**a**) on soft substrates and their mechanosensitivity (**b**) (Methods). Mechanosensitivity is defined as $(N/C)_{\text{stiff}}/(N/C)_{\text{soft}}$. **c-e**, Representative examples of construct distribution in cells seeded in substrates of 1.5 kPa or 30 kPa, for L-NLS constructs at different MW, M-NLS constructs at different MW, and 41 kDa constructs at different NLS strengths. **f-h**, N/C ratios corresponding to the same conditions as **c-e**. **i-k**, Mechanosensitivity corresponding to the same conditions as **c-e**. **l,m**, Kinetic model predictions of N/C ratios (**l**) and mechanosensitivities (**m**) for NLS of different affinities for importin α (modelled through the binding rates k_{on} between the NLS and importin α, with values of 54 and 205 ms^{-1}) as a function of MW. **n,o**, Model predictions of N/C ratios (**n**) and mechanosensitivities (**o**) for 41 kDa constructs, as a function of increasing NLS strength. Statistics: in **f**, $N=120$ cells from three independent experiments, both MW ($P<1\times 10^{-15}$) and stiffness ($P<1\times 10^{-15}$) effects tested significant; in **g**, $N=120$ cells from three independent experiments, both MW ($P<1\times 10^{-15}$) and stiffness ($P=0.0015$) effects tested significant; in **h**, $N=120$ cells from three independent experiments, both NLS strength ($P<1\times 10^{-15}$) and stiffness ($P=0.0012$) effects tested significant. Two-way ANOVA, Šídák's multiple comparisons test was used to obtain P values between conditions. Scale bars, 20 μm. Data are mean \pm s.e.m. Source numerical data are available in source data.

developed constructs by combining PrA repeats with different NES signals of different strength⁴⁵ (Supplementary Table 2). N/C ratios changed as expected with MW and NES strength (by following the opposite trends than NLS constructs, Fig. 5a–i). The mechanosensitivity of the constructs also behaved in the opposite way, with constructs leaving (rather than entering) the nucleus with force

(Fig. 5g–i). Consistently, influx and efflux rates of NES constructs also had opposite trends with MW than NLS constructs: efflux rates were largely independent of MW, whereas influx rates showed a strong dependence, mimicking diffusive constructs (Extended Data Fig. 5a, b). Confirming the effect of force, applying force to the nucleus with AFM to the most mechanosensitive NES construct



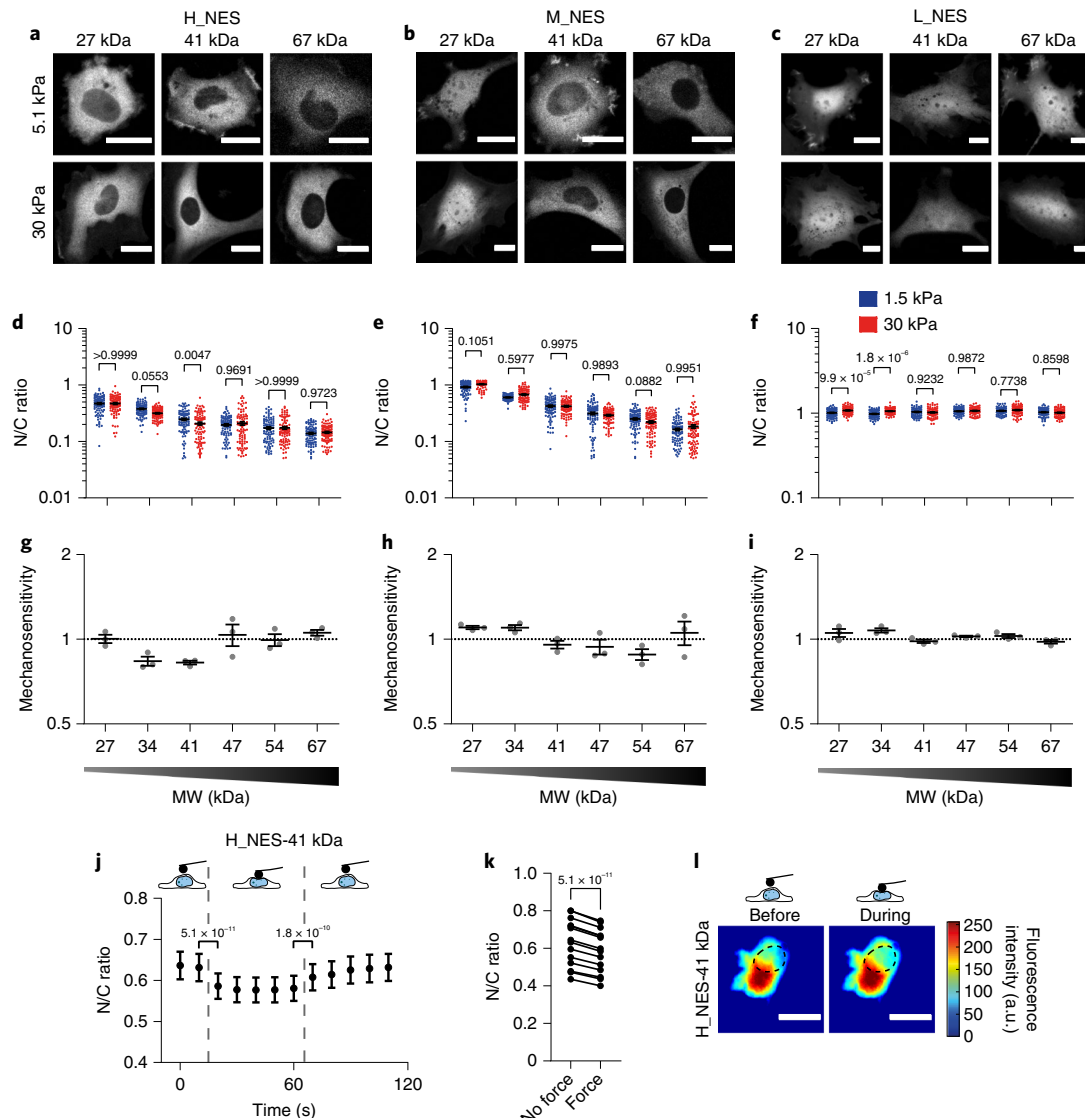


Fig. 5 | Balance between affinity to exportin 1 and MW defines the mechanosensitivity of nuclear localization in constructs containing NES signals.

a-c, Representative examples of construct distribution in cells seeded in substrates of 1.5 kPa or 30 kPa, for H_NES constructs at different MW, M_NES constructs at different MW and L_NES constructs at different MW.

d-f, N/C ratios corresponding to the same conditions as a-c. **d**, $N=90$ cells from three independent experiments. Both MW ($P<1\times 10^{-15}$) and stiffness ($P=0.0162$) effects tested significant. **e**, $N=120$ cells from three independent experiments. Only MW effects tested significant ($P<1\times 10^{-15}$). **f**, $N=90$ cells from three independent experiments. Both MW ($P<1\times 10^{-15}$) and stiffness ($P=0.0001$) effects tested significant. Two-way ANOVA, Šídák's multiple comparisons test was used to obtain P values between conditions.

g-i, Mechanosensitivity corresponding to the same conditions as a-c. Mechanosensitivity is defined as $(N/C)_{\text{stiff}}/(N/C)_{\text{soft}}$ ($n=3$ experiments).

j, N/C ratios of H_NES 41 kDa construct in cells seeded on 1.5 kPa gels before, during and after nuclear deformation with AFM.

k, From data in j, paired dot plots of the timepoints right before and after force application. In j and k, $N=15$ cells from three independent experiments. P values were calculated with a two-tailed paired t-test; traces of all cells are shown in Extended Data Fig. 8.

l, Corresponding images of constructs before and during force application; dotted line marks nucleus outline. Scale bars, 20 μ m. Data are mean \pm s.e.m. Source numerical data are available in source data.

(H_NES-EGFP-2PrA 41 KDa) led to a reduction of N/C ratios (Fig. 5j-l). Interestingly, mechanosensitivity of the NES constructs was systematically milder than that of the NLS constructs. This is consistent with the behaviour of the light-inducible construct (Fig. 1b), which had a stiffness-dependent localization when controlled by active import (no light excitation) but not when controlled by active export (under light excitation). This lower mechanosensitivity of active export as compared with import may be related to the many differences between the transport cycles in both directions, and particularly the fact that NES-mediated export, unlike NLS-mediated import, is directly coupled to the hydrolysis of Ran-GTP^{30,42,46}. However, another potential intuitive explanation

could be that a concentration gradient is more easily generated by accumulating proteins in a small compartment (the nucleus) than a large one (the cytoplasm). In line with this hypothesis, model predictions obtained by inverting nuclear and cytoplasmic volumes led to lower N/C ratios and mechanosensitivity (Extended Data Fig. 6).

Mechanosensitivity of transcriptional regulators. Finally, we evaluated whether nucleocytoplastic transport can explain the reported mechanosensitivity of different transcriptional regulators. Different transcriptional regulators localize to the nucleus with force in different contexts, including YAP^{6,47}, twist1 (ref. ⁴⁸), snail⁴⁹, SMAD3 (ref. ⁵⁰), GATA2 (ref. ⁵¹) and NFκB⁵². If their mechanosensitivity

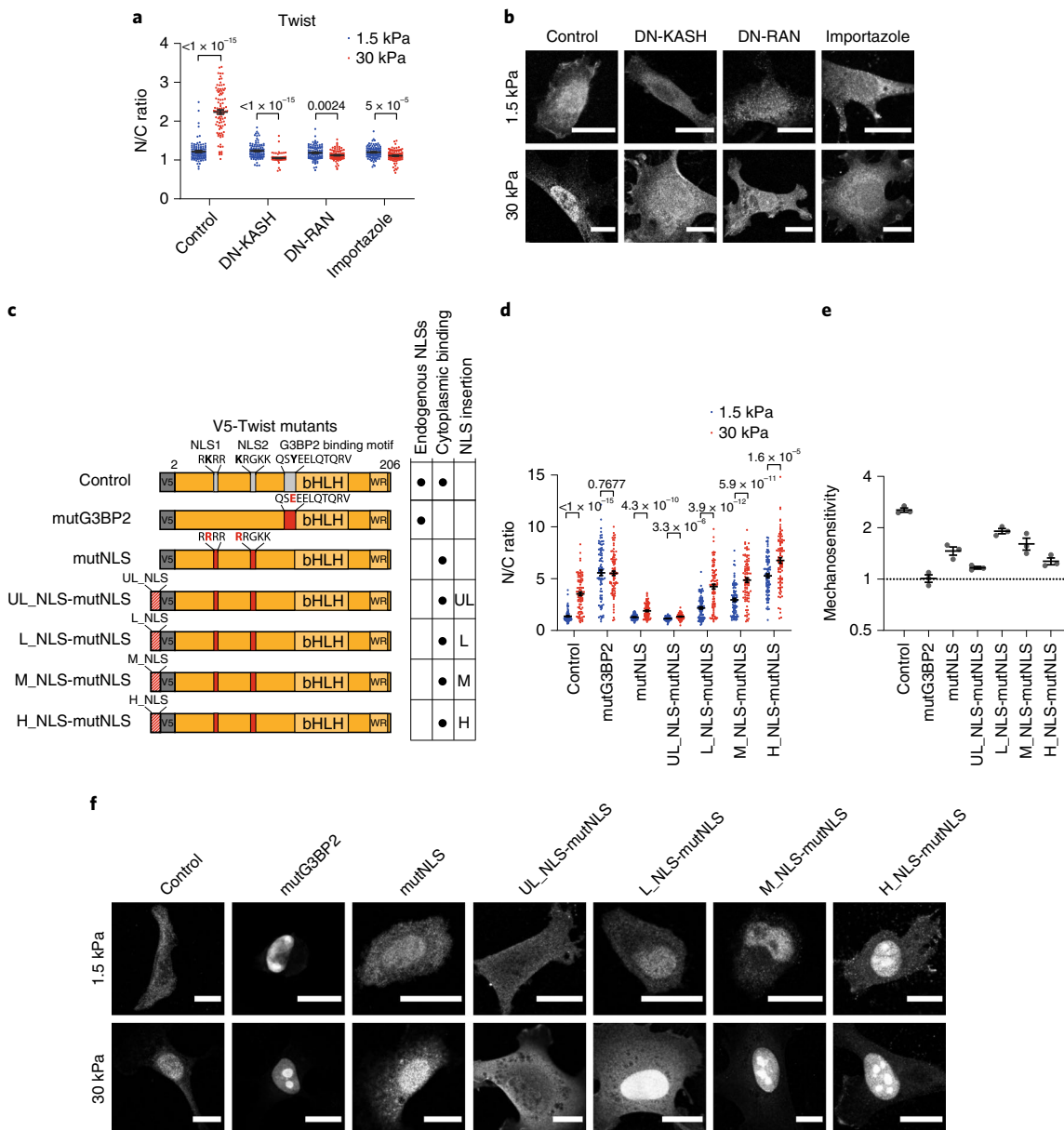


Fig. 6 | The mechanosensitivity of *twist1* can be re-engineered with exogenous NLS sequences. **a**, N/C ratios of endogenous *twist1* for cells on 1.5 kPa and 30 kPa substrates, and under indicated treatments. $N=100$ cells from three independent experiments. P values from two-tailed Mann-Whitney tests, corrected for multiple tests in the intra-condition comparisons with the two-stage step-up method of Benjamini, Krieger and Yekutieli. **b**, Corresponding images of *twist1* distribution. **c**, Scheme of different *twist1* mutants. Mutations inactivating both NLS sequences and the G3BP2 binding motif are indicated in red. **d**, N/C ratios of transfected *twist1* mutants for cells on 1.5 kPa or 30 kPa substrates. $N=90$ cells from three independent experiments. P values from two-tailed Mann-Whitney tests, corrected for multiple tests with the two-stage step-up method of Benjamini, Krieger and Yekutieli. **e**, Corresponding construct mechanosensitivities, defined as $(N/C)_{\text{stiff}}/(N/C)_{\text{soft}}$ ($N=3$ experiments). **f**, Corresponding images showing the distribution of the different mutants. Scale bars, 20 μ m. Data are mean \pm s.e.m. Source numerical data are available in source data.

is explained by regulation of nucleocytoplasmic transport with nuclear force, then it should be abolished by preventing either force transmission to the nucleus (by overexpressing DN-KASH) or nucleocytoplasmic transport (by overexpressing either DN-Ran, a dominant-negative version of Ran⁵³, or by treatment with importazole, a drug that blocks active import by importin β ⁵⁴). For the case of YAP, we previously showed that its mechanosensitivity is abrogated by both factors⁶. Regarding the rest, GATA2 and NF κ B exhibited a very low mechanosensitivity in our system (Extended Data Fig. 7), but SMAD3, Snail and Twist1 showed a clear response (Fig. 6a,b and Extended Data Fig. 7). In all cases, mechanosensitivity

was abrogated by DN-KASH, DN-Ran or importazole (Fig. 6a,b and Extended Data Fig. 7). Interestingly, and consistent with our finding that NLS constructs were more mechanosensitive than NES constructs, SMAD3 mechanosensitivity was higher for cells treated with TGF β (which induces SMAD3 nuclear import) than with lapatinib (which induces SMAD3 nuclear export)⁵⁵.

Thus, the mechanosensitivity of several transcriptional regulators is controlled by force-induced effects in nucleocytoplasmic transport. Our proposed mechanism also has the stronger implication that mechanosensitivity can be engineered simply by selecting the appropriate levels of affinity to importins. To verify this, we took

twist1 as a convenient model, since its NLS sequences are known, and their function can be abolished with point mutations⁵⁶. Further, its mechanosensitivity depends on its binding to G3BP2, which retains *twist1* in the cytoplasm⁴⁸. We first overexpressed wild-type *twist1* in cells, which retained the mechanosensitivity of endogenous *twist1* (Fig. 6c–f). Of note, changes in *twist1* caused by either stiffness or overexpression did not consistently increase the expression of *twist1* target genes (Extended Data Fig. 7). Thus, *twist1* serves as a model for protein localization but not transcription. Then, we overexpressed a G3BP2-binding-deficient mutant, mutG3BP2. As expected, this led to high N/C ratios on both soft and stiff substrates, thereby losing mechanosensitivity. Confirming the role of nucleocytoplasmic transport, the NLS dead mutant (mutNLS, still under the control of G3BP2), lost the nuclear localization in both soft and stiff substrates, thereby also losing mechanosensitivity (although not completely; Fig. 6c–f). We then assessed whether we could restore *twist1* mechanosensitivity by rescuing twist mutNLS not with its endogenous NLS, but by exogenously adding our different characterized NLS sequences (plus an additional ultra-low affinity sequence, UL_NLS). Adding NLS sequences of different strength mimicked the effects seen in Fig. 4: as the NLS strength increased, nuclear localization progressively increased, and mechanosensitivity was highest at a low strength (L_NLS), where it was almost as high as in the endogenous case. Thus, simply substituting the endogenous *twist1* NLS with an exogenous one of the appropriate strength, not regulated by any *twist1*-related signalling mechanism, recapitulates its mechanosensitivity.

Discussion

Our work shows that force regulates nucleocytoplasmic transport by weakening the permeability barrier of NPCs, affecting both passive and facilitated diffusion. As MW affects passive diffusion more than facilitated diffusion, this generates a differential effect on both types of transport that enables force-induced nuclear (or cytosolic) localization of cargo. The mechanical weakening of the permeability barrier is most likely the consequence of NPC deformation, and we previously reported increased apparent NPC diameters for cells on stiff versus soft substrates⁶. Further, recent structural evidence has confirmed the deformability of NPCs. In NPCs, the meshwork of FG Nup proteins that conforms the permeability barrier is supported by the NPC inner ring, which is formed by eight symmetric spokes^{57,58}. Spokes have limited interactions with each other through flexible linker proteins⁵⁹. This allows NPCs to dilate or constrict by changing the distance between spokes, as proposed a decade ago⁶⁰ and as verified very recently^{61,62}. Such dilation and constriction indeed occur in response to energy depletion or to changes in osmotic pressure, probably in response to changes in nuclear membrane tension⁶¹. This proposed direct regulation of NPC permeability with force is strongly supported by the immediate response observed in AFM experiments, the effects observed in passive diffusion and the dependency on MW. On top of this mechanism, indirect effects mediated for instance by changes in importin α levels (Extended Data Fig. 3) or by competition between cargoes for importin binding (as recently demonstrated between YAP and importin 7 (ref. ⁶³)) may play a role in different contexts.

Three important open questions emerge from our findings. First, how mechanical deformation of NPCs weakens the permeability barrier of FG Nups in both passive and facilitated diffusion remains to be understood. The LINC complex may play an important role, as suggested by the fact that responses to stiffness (in which cells apply force to the nucleus through the cytoskeleton and the LINC complex) are larger than responses to more unspecific force application with an AFM. This is further supported by the abrogation of AFM responses upon DN-KASH overexpression. Second, the exact set of properties that confer mechanosensitivity to transcriptional regulators or other proteins remains to be fully explored. The different

transcriptional regulators discussed here range in size from over 20 kDa (for *twist*) to over 60 kDa (for YAP), thereby encompassing almost the full range of weights analysed with our designed constructs. However, diffusivity through NPCs depends not only on MW but also on surface charges⁶⁴ and protein mechanical properties⁶⁵, which could play major roles. Finally, why facilitated export is less affected than facilitated import may be related to the different volumes of nucleus and cytoplasm (as suggested by modelling in Extended Data Fig. 6), to the different interactions between importins and exportins with FG Nups⁶⁶ or to the asymmetric manner in which NPCs deform⁶¹.

Our work demonstrates a general mechanism of mechanosensitivity, with incorporated specificity through molecular properties such as the NLS sequence and MW. Although other mechanisms (such as differential binding to nuclear or cytosolic proteins) can generate mechanosensitive nuclear translocation^{14,16}, our mechanism is consistent with the behaviour of several transcriptional regulators, and has potential general applicability. Our findings suggest that interfering with nucleocytoplasmic transport may be an avenue to regulate or abrogate mechanically induced transcription in several pathological conditions. Perhaps even more excitingly, they open the door to designing artificial mechanosensitive transcription factors, to enable mechanical control of transcriptional programmes at will.

Online content

Any methods, additional references, Nature Research reporting summaries, source data, extended data, supplementary information, acknowledgements, peer review information; details of author contributions and competing interests; and statements of data and code availability are available at <https://doi.org/10.1038/s41556-022-00927-7>.

Received: 17 September 2021; Accepted: 26 April 2022;
Published online: 9 June 2022

References

1. Broders-Bondon, F., Ho-Bouloire, T. H. N., Fernandez-Sanchez, M. E. & Farge, E. Mechanotransduction in tumor progression: the dark side of the force. *J. Cell Biol.* **217**, 1571–1587 (2018).
2. Hamant, O. & Saunders, T. E. Shaping organs: shared structural principles across kingdoms. *Annu. Rev. Cell Dev. Biol.* **36**, 385–410 (2020).
3. Humphrey, J. D., Schwartz, M. A., Tellides, G. & Milewicz, D. M. Role of mechanotransduction in vascular biology: focus on thoracic aortic aneurysms and dissections. *Circ. Res.* **116**, 1448–1461 (2015).
4. Lombardi, M. L. et al. The interaction between nesprins and sun proteins at the nuclear envelope is critical for force transmission between the nucleus and cytoskeleton. *J. Biol. Chem.* **286**, 26743–26753 (2011).
5. Arsenovic, P. T. et al. Nesprin-2G, a component of the nuclear LINC complex, is subject to myosin-dependent tension. *Biophys. J.* **110**, 34–43 (2016).
6. Elosgui-Artola, A. et al. Force triggers YAP nuclear entry by regulating transport across nuclear pores. *Cell* **171**, 1397–1410 e14 (2017).
7. Kirby, T. J. & Lammerding, J. Emerging views of the nucleus as a cellular mechanosensor. *Nat. Cell Biol.* **20**, 373–381 (2018).
8. Nava, M. M. et al. Heterochromatin-driven nuclear softening protects the genome against mechanical stress-induced damage. *Cell* **181**, 800–817.e22 (2020).
9. Tajik, A. et al. Transcription upregulation via force-induced direct stretching of chromatin. *Nat. Mater.* **15**, 1287–1296 (2016).
10. Swift, J. et al. Nuclear lamin-A scales with tissue stiffness and enhances matrix-directed differentiation. *Science* **341**, 1240104 (2013).
11. Lomakin, A. J. et al. The nucleus acts as a ruler tailoring cell responses to spatial constraints. *Science* **370**, eaba2894 (2020).
12. Venturini, V. et al. The nucleus measures shape changes for cellular proprioception to control dynamic cell behavior. *Science* **370**, eaba2644 (2020).
13. Kassianidou, E., Kalita, J. & Lim, R. Y. H. The role of nucleocytoplasmic transport in mechanotransduction. *Exp. Cell. Res.* **377**, 86–93 (2019).
14. Zhao, X. H. et al. Force activates smooth muscle α -actin promoter activity through the Rho signaling pathway. *J. Cell Sci.* **120**, 1801–1809 (2007).
15. Ho, C. Y., Jaalouk, D. E., Virtanen, M. K. & Lammerding, J. Lamin A/C and emerin regulate MKL1-SRF activity by modulating actin dynamics. *Nature* **497**, 507–511 (2013).

16. Fernandez-Sanchez, M. E. et al. Mechanical induction of the tumorigenic β -catenin pathway by tumour growth pressure. *Nature* **523**, 92–95 (2015).
17. Gayrard, C., Bernaudin, C., Dejardin, T., Seiler, C. & Borghi, N. Src- and confinement-dependent FAK activation causes E-cadherin relaxation and β -catenin activity. *J. Cell Biol.* **217**, 1063–1077 (2018).
18. Aragona, M. et al. Mechanisms of stretch-mediated skin expansion at single-cell resolution. *Nature* **584**, 268–273 (2020).
19. Chang, L. et al. The SWI/SNF complex is a mechanoregulated inhibitor of YAP and TAZ. *Nature* **563**, 265–269 (2018).
20. Ege, N. et al. Quantitative analysis reveals that actin and src-family kinases regulate nuclear YAP1 and its export. *Cell Syst.* **6**, 692–708.e13 (2018).
21. Jacchetti, E. et al. The nuclear import of the transcription factor MyoD is reduced in mesenchymal stem cells grown in a 3D micro-engineered niche. *Sci. Rep.* **11**, 1–19 (2021).
22. SR, W. & MP, R. The nuclear pore complex and nuclear transport. *Cold Spring Harb. Perspect. Biol.* **2**, a000562 (2010).
23. M, B. & E, H. The nuclear pore complex: understanding its function through structural insight. *Nat. Rev. Mol. Cell Biol.* **18**, 73–89 (2017).
24. Paine, P. L. & Feldherr, C. M. Nucleocytoplasmic exchange of macromolecules. *Exp. Cell. Res.* **74**, 81–98 (1972).
25. Timney, B. L. et al. Simple rules for passive diffusion through the nuclear pore complex. *J. Cell Biol.* **215**, 57–76 (2016).
26. Mohr, D., Frey, S., Fischer, T., Gütter, T. & Görlich, D. Characterisation of the passive permeability barrier of nuclear pore complexes. *EMBO J.* **28**, 2541–2553 (2009).
27. Denning, D. P., Patel, S. S., Uversky, V., Fink, A. L. & Rexach, M. Disorder in the nuclear pore complex: the FG repeat regions of nucleoporins are natively unfolded. *Proc. Natl Acad. Sci. USA* **100**, 2450–2455 (2003).
28. Yuh, M. C. & Blobel, G. Karyopherins and nuclear import. *Curr. Opin. Struct. Biol.* **11**, 703–715 (2001).
29. Nachury, M. V. & Weis, K. The direction of transport through the nuclear pore can be inverted. *Proc. Natl Acad. Sci. USA* **96**, 9622–9627 (1999).
30. Cautain, B., Hill, R., De Pedro, N. & Link, W. Components and regulation of nuclear transport processes. *FEBS J.* **282**, 445–462 (2015).
31. Kalderon, D., Roberts, B. L., Richardson, W. D. & Smith, A. E. A short amino acid sequence able to specify nuclear location. *Cell* **39**, 499–509 (1984).
32. Görlich, D. Transport into and out of the cell nucleus. *EMBO J.* **17**, 2721–2727 (1998).
33. Wente, S. R. & Rout, M. P. The nuclear pore complex and nuclear transport. *Cold Spring Harb. Perspect. Biol.* **2**, a000562 (2010).
34. Niopek, D., Wehler, P., Roensch, J., Eils, R. & Di Ventura, B. Optogenetic control of nuclear protein export. *Nat. Commun.* **7**, 1–9 (2016).
35. Elosegui-Artola, A. et al. Mechanical regulation of a molecular clutch defines force transmission and transduction in response to matrix rigidity. *Nat. Cell Biol.* **18**, 540–548 (2016).
36. Schiller, H. B. et al. β 1- and α v-class integrins cooperate to regulate myosin II during rigidity sensing of fibronectin-based microenvironments. *Nat. Cell Biol.* **15**, 625–636 (2013).
37. Hodel, M. R., Corbett, A. H. & Hodel, A. E. Dissection of a nuclear localization signal. *J. Biol. Chem.* **276**, 1317–1325 (2001).
38. Lyman, S. K., Guan, T., Bednenko, J., Wodrich, H. & Gerace, L. Influence of cargo size on Ran and energy requirements for nuclear protein import. *J. Cell Biol.* **159**, 55–67 (2002).
39. Ribbeck, K. & Görlich, D. The permeability barrier of nuclear pore complexes appears to operate via hydrophobic exclusion. *EMBO J.* **21**, 2664–2671 (2002).
40. Lowe, A. R. et al. Selectivity mechanism of the nuclear pore complex characterized by single cargo tracking. *Nature* **467**, 600–603 (2010).
41. Kopito, R. B. & Elbaum, M. Nucleocytoplasmic transport: a thermodynamic mechanism. *HFSP J.* **3**, 130–141 (2010).
42. Kim, S. & Elbaum, M. A simple kinetic model with explicit predictions for nuclear transport. *Biophys. J.* **105**, 565–569 (2013).
43. Jovanovic-Talisman, T. & Zilman, A. Protein transport by the nuclear pore complex: Simple biophysics of a complex biomachine. *Biophys. J.* **113**, 6–14 (2017).
44. Görlich, D., Seewald, M. J. & Ribbeck, K. Characterization of Ran-driven cargo transport and the RanGTPase system by kinetic measurements and computer simulation. *EMBO J.* **22**, 1088–1100 (2003).
45. Kanwal, C., Mu, S., Kern, S. E. & Lim, C. S. Bidirectional on/off switch for controlled targeting of proteins to subcellular compartments. *J. Control. Release* **98**, 379–393 (2004).
46. Kim, S. & Elbaum, M. Enzymatically driven transport: a kinetic theory for nuclear export. *Biophys. J.* **105**, 1997–2005 (2013).
47. Dupont, S. et al. Role of YAP/TAZ in mechanotransduction. *Nature* **474**, 179–183 (2011).
48. Wei, S. C. et al. Matrix stiffness drives epithelial–mesenchymal transition and tumour metastasis through a TWIST1–G3BP2 mechanotransduction pathway. *Nat. Cell Biol.* **17**, 678–688 (2015).
49. Zhang, K. et al. Mechanical signals regulate and activate SNAI1 protein to control the fibrogenic response of cancer-associated fibroblasts. *J. Cell Sci.* **129**, 1989–2002 (2016).
50. Furumatsu, T. et al. Mechanical stretch increases Smad3-dependent CCN2 expression in inner meniscus cells. *J. Orthop. Res.* **30**, 1738–1745 (2012).
51. Mammoth, A. et al. A mechanosensitive transcriptional mechanism that controls angiogenesis. *Nature* **457**, 1103–1108 (2009).
52. Ishihara, S. et al. Substrate stiffness regulates temporary NF- κ B activation via actomyosin contractions. *Exp. Cell. Res.* **319**, 2916–2927 (2013).
53. Bischoff, F. R., Klebe, C., Kretschmer, J., Wittinghofer, A. & Ponstingl, H. RanGAP1 induces GTPase activity of nuclear Ras-related Ran. *Proc. Natl Acad. Sci. USA* **91**, 2587–2591 (1994).
54. Soderholm, J. F. et al. Importazole, a small molecule inhibitor of the transport receptor importin- β . *ACS Chem. Biol.* **6**, 700–708 (2011).
55. F, H. et al. HER2/EGFR-AKT signaling switches TGF β from inhibiting cell proliferation to promoting cell migration in breast cancer. *Cancer Res.* **78**, 6073–6085 (2018).
56. Singh, S. & Gramolini, A. O. Characterization of sequences in human TWIST required for nuclear localization. *BMC Cell Biol.* **10**, 47 (2009).
57. Lin, D. H. et al. Architecture of the symmetric core of the nuclear pore. *Science* **352**, aaf1015 (2016).
58. Kosinski, J. et al. Molecular architecture of the inner ring scaffold of the human nuclear pore complex. *Science* **352**, 363–365 (2016).
59. Petrovic, S. et al. Architecture of the linker-scaffold in the nuclear pore. *bioRxiv* <https://doi.org/10.1101/2021.10.26.465796> (2021).
60. Hoelz, A., Debler, E. W. & Blobel, G. The structure of the nuclear pore complex. *Annu. Rev. Biochem.* **80**, 613–643 (2011).
61. Zimmerli, C. E. et al. Nuclear pores dilate and constrict in cellulose. *Science* **374**, eabd9776 (2021).
62. Schuller, A. P. et al. The cellular environment shapes the nuclear pore complex architecture. *Nature* **598**, 667–671 (2021).
63. García-García, M. et al. Mechanical control of nuclear import by Importin-7 is regulated by its dominant cargo YAP. *Nat. Commun.* **13**, 1–21 (2022).
64. Frey, S. et al. Surface properties determining passage rates of proteins through nuclear pores. *Cell* **174**, 202–217.e9 (2018).
65. Infante, E. et al. The mechanical stability of proteins regulates their translocation rate into the cell nucleus. *Nat. Phys.* **15**, 973–981 (2019).
66. Aramburu, I. V. & Lemke, E. A. Floppy but not sloppy: interaction mechanism of FG-nucleoporins and nuclear transport receptors. *Semin. Cell Dev. Biol.* **68**, 34–41 (2017).

Publisher's note Springer Nature remains neutral with regard to jurisdictional claims in published maps and institutional affiliations.

© The Author(s), under exclusive licence to Springer Nature Limited 2022

Methods

Cell culture and reagents. Mouse embryonic fibroblasts were cultured as previously described⁶⁷, using Dulbecco's modified Eagle medium (DMEM; Thermo Fisher Scientific, 41965-039) supplemented with 10% v/v FBS (Thermo Fisher Scientific, 10270-106), 1% v/v penicillin–streptomycin (Thermo Fisher Scientific, 10378-016) and 1.5% v/v HEPES 1 M (Sigma Aldrich, H0887). Cell cultures were routinely checked for mycoplasma. CO₂-independent medium was prepared by using CO₂-independent DMEM (Thermo Fisher Scientific, 18045 –054) supplemented with 10% v/v FBS, 1% v/v penicillin–streptomycin, 1.5% v/v HEPES 1 M and 2% v/v L-glutamine (Thermo Fisher Scientific, 25030-024). Medium for AFM experiments was supplemented with rutin (Thermo Fisher Scientific, 132391000) 10 mg l⁻¹ right before the experiment. Importazole (Sigma Aldrich) was used at 40 μM concentration for 1 h (ref. ⁵⁴). Cells were transfected the day before the experiment using Neon transfection device (Thermo Fisher Scientific) according to the manufacturer's instructions. Cells were seeded ~4 h before the experiment.

Antibodies and compounds. For primary antibodies, we used Anti Twist antibody (Twist2C1A, Santa Cruz, sc-81417, RRID:AB_1130910) 1:200, mouse monoclonal antibody to SNAI1 + SLUG N-terminal (clone number CL3700; abcam, ab224731) 1:200, rabbit polyclonal anti SMAD3 (Cell Signaling, 9513, RRID: AB_2286450) 1:40, rabbit polyclonal antibody to GATA2 (Abcam, ab153820) 1:200, rabbit polyclonal anti-NF-kB p65 antibody (abcam, ab16502, RRID: AB_443394) 1:200, KPNA4/importin α 3 (NPBP1-31260 Novus Biologicals, RRID: AB_2133841) 1:200, KPNA2/importin α 1 (MAB6207 Bio-techne, clone number 682239) 1:200, and KPNB1/importin β 1 (ab2811 Abcam, RRID: AB_2133989) 1:200. The secondary antibodies used were Alexa Fluor 488 anti-mouse (A-11029; Thermo Fisher Scientific, RRID: AB_2534088) and Alexa Fluor 555 anti-rabbit (A-21429; Thermo Fisher Scientific, RRID: AB_2535850) diluted 1:200.

If not specified otherwise, plasmids were constructed via standard molecular biology methods. LEXY plasmids: NLS-mCherry-LEXY (pDN122) was a gift from Barbara Di Ventura and Roland Eils (Addgene plasmid number 72655; <http://n2t.net/addgene:72655>; RRID: Addgene_72655) (ref. ³⁴). Nuclear transport plasmids: NLS, NES or nought combinations with different MW modules were designed as follows: localization signal plus GGGGS linker, EGFP and different repeats of protein A (PrA) from *Staphylococcus aureus* modules. NLS sequences were extracted from ref. ³⁷. NES sequences were extracted from ref. ⁴⁵. Protein A domain sequences were used originally in ref. ²⁵ and were kindly provided by M. Rout. NLS and NES insertions were performed following the protocol of Liu and Naishith⁶⁸. PrA insertions plasmid were constructed via Gibson Assembly protocol, as well as BFP plasmid from IG062. For more detailed information, see Supplementary Tables 1 and 2. DN-KASH DN-RAN: DN-KASH was described previously as EGFP-Nesprin1-KASH in ref. ⁶⁹. DN-RAN (Addgene plasmid number 30309, described as pmCherry-C1-RanQ69L) was a gift from Jay Brennan⁷⁰. Twist mutants: pBABE-puro-mTwist was a gift from Bob Weinberg (Addgene plasmid number 1783; <http://n2t.net/addgene:1783>; RRID: Addgene_1783) (ref. ⁷¹). mTwist was cloned into a pEGFP-C3 backbone, and a V5 tag was included at the N-terminal. The different mutants were constructed by adding the corresponding NLS sequences and/or changing the indicated codons. For more detailed information, see Supplementary Table 1.

Polyacrylamide gels. Polyacrylamide gels were prepared as previously described⁷², and coated using a protocol adapted from the literature³. Gels were prepared by mixing acrylamide (5.5% or 12% v/v for 1.5 kPa or 30 kPa gels, respectively) and bis-acrylamide (0.04% or 0.15% v/v for 1.5 kPa or 30 kPa gels, respectively) with 2% v/v 200-nm-diameter dark-red fluorescence carboxylate-modified beads (Fluospheres, Thermo Fisher Scientific), 0.5% v/v ammonium persulfate (Sigma Aldrich) and 0.05% tetramethylmethylenediamine (Sigma Aldrich), in PBS 1×. A drop of 22 μl was placed on top of a glass bottom well and then sandwiched with an 18 mm diameter coverslip. Gels were then kept at room temperature for 45 min to polymerize. Finally, gels were covered in PBS 1× and the top coverslip was removed. To coat gels, we first prepared a mixture containing HEPES (0.5 M, pH 6, 10% v/v), acrylamide and bis-acrylamide (BioRad), N-hydroxysuccinimide (0.3% v/v from an initial solution of 10 mg ml⁻¹ in dimethyl sulfoxide, Sigma Aldrich), Irgacure 2959 (1% v/v, BASF) and di(trimethylolpropane)tetra-acrylate (0.0012% v/v, Sigma Aldrich), in Milli-Q water. This mixture was placed on top of gels, and gels were then illuminated with UV light for 10 min. After exposure, gels were washed once with HEPES 25 mM pH 6 and once with PBS. Gels were then incubated with 10 μg ml⁻¹ of fibronectin in PBS overnight at 4 °C, UV-treated in the hood for 10 min, washed once with PBS and immediately used. The rigidity (Young's modulus) of the gels was measured as previously described⁷⁴ using a Nanowizard 4 AFM (JPK). Silicon nitride pyramidal tips with an effective half angle θ of 20° and a nominal spring constant of $k=0.01\text{ N m}^{-1}$ were used (MLCT, Bruker). The spring constant of the cantilevers was calibrated by thermal tuning using the simple harmonic oscillator model. Force–displacement curves with a peak-to-peak amplitude of 6 μm and a frequency of 1 Hz were acquired. Sixty-four points near the gel centre were selected in each gel, separated 5 μm from each other. Eight gels produced in two batches were measured for each stiffness. To compute the Young's modulus (E), the Hertz model equation for pyramidal tips was fitted

to the force–displacement curves, using the JPK software (JPK Data Processing Version 6.1.79). The equation was fitted for an effective indentation of 500 nm.

Immunostaining. Immunostainings were performed as previously described⁶. Cells were fixed with 4% v/v paraformaldehyde for 10 min, permeabilized with 0.1% v/v Triton X-100 for 40 min, blocked with 2% v/v fish gelatin in PBS 1× for 40 min, incubated with primary antibody for 1 h, washed three times with fish-gelatin–PBS for 5 min, incubated with secondary antibody for 1 h, washed with fish-gelatin–PBS 3× for 5 min and mounted using ProLong Gold Antifade Mountant (Thermo Fisher Scientific).

Real-time PCR experiments. Real-time PCR experiments were performed according to the manufacturer's instructions (Applied Biosystems). Total mRNA was extracted from cells in the different conditions using the Qiagen RNeasy Micro Kit. Concentration of the obtained mRNA was measured with a Nanodrop ND-1000 Spectrophotometer. Equal amounts of RNA samples were reverse-transcribed into complementary DNA using the iScript cDNA Synthesis Kit. SYBR Green (Applied Biosystems 4385612) RT-qPCRs were performed in triplicates with a StepOnePlus System (Applied Biosystems) under standard conditions. The $2^{-\Delta\Delta Ct}$ method was used to calculate relative gene expression. All ΔΔCt values were normalized to the housekeeping gene GAPDH. Primer sequences for the different measured genes are detailed in Supplementary Table 3.

Steady-state image acquisition and analysis. Cells were imaged with a Nikon Eclipse Ti inverted confocal microscope with Micromanager (version 1.4.22), using a 60× water immersion objective 1.2 NA. Microscopy images were acquired by using Zeiss ZEN2.3 SP1 FP3 (black, version 14.0.24.201) or Micromanager (version 1.4.22). N/C ratios were quantified manually by segmenting the nucleus using Hoechst (immunostaining) or taking advantage of the GFP-tagged construct (live cells) by the following formula:

$$\frac{N}{C} = \frac{I_{\text{nucleus}} - I_{\text{background}}}{I_{\text{cytoplasm}} - I_{\text{background}}}$$

Where I_{nucleus} and $I_{\text{cytoplasm}}$ are the mean fluorescence intensity of the nucleus and the cytoplasm, respectively. Regions of interest (ROIs) in the nucleus and in the cytoplasm were selected manually next to each other, close to the nuclear membrane. $I_{\text{background}}$ is the mean intensity of the background far from the cell.

Mechanosensitivity was calculated once for each of the experimental repeats using the following formula:

$$\text{mechanosensitivity} = \frac{[\text{N/C stiff substrate}]}{[\text{N/C soft substrate}]}$$

Where [N/C stiff substrate] and [N/C soft substrate] are the average N/C ratios on stiff/soft substrates for all cells within the experimental repeat. These quantifications were done by using ImageJ software (version 1.53e).

Live-cell AFM experiments. Live-cell AFM experiments were carried out as previously described⁶. AFM experiments were carried out in a Nanowizard 4 AFM (JPK) mounted on top of a Nikon Ti Eclipse microscope, using the JPK software (JPK Data Processing Version 6.1.79). Polystyrene beads of 20 μm were attached using a non-fluorescent adhesive (NOA63, Norland Products) to the end of tipless MLCT cantilevers (Veeco). The spring constant of the cantilevers was calibrated by thermal tuning using the simple harmonic oscillator model. Experiments were carried out on cells previously transfected with the different constructs indicated in figures, incubated with Hoechst 33342 (Invitrogen), and seeded on 1.5 kPa gels. For each cell, the nucleus was identified by using the Hoechst fluorescence signal, and a force of 1.5 nN was applied to the nucleus. Once the maximum force was reached, the indentation was kept constant under force control, adjusting the z height by feedback control. An image was acquired every 10 s by an Orca ER camera (Hamamatsu) and a 60× (NA 1.2) objective.

Photoactivation experiment and quantification. Photoactivation experiments were done with a Zeiss LSM880 inverted confocal microscope using a 63× 1.46 NA oil immersion objective and using Zeiss ZEN2.3 SP1 FP3 (black, version 14.0.24.201). An argon laser was used with 561 nm wavelength for acquisition and 488 nm laser for stimulation. For experiments, four images were obtained before stimulation, followed by 19 images during stimulation, and 18 images during recovery. All images were acquired every 30 s. During the stimulation period, the 488 nm laser was irradiated to the whole field of view also every 30 s, during 1 s at 100% laser power.

To obtain the entry and exit coefficient, a single exponential equation was fitted to the N/C ratio of each cell:

$$n/c(t) = (n/c)_0 e^{-kt}$$

Where $(n/c)_0$ is the initial ratio of the stimulation or recovery phase, t is time and k is the entry or exit coefficient. The curve was fitted to the whole stimulation or recovery phase.

FRAP data acquisition and analysis. Estimation of mobile fraction of proteins was done using fluorescence recovery after photobleaching (FRAP) experiments. FRAP involves bleaching an ROI and then tracing the recovery of fluorescence in that region with respect to time. Image acquisition was done with a Zeiss LSM880 inverted confocal microscope objective and using Zeiss ZEN2.3 SP1 FP3 (black, version 14.0.24.201), using a 63×1.46 NA oil immersion objective and a 488 nm wavelength argon laser at 100% laser power. We acquired images every 60 ms, before and after bleaching. We use two ROIs for our experiments: first, the circular 14-pixel diameter ($\sim 6.9 \mu\text{m}^2$) region being bleached (ROIF). Second, the cell area segmented manually (ROIC). The data for ROIs consist of the fluorescence integrated density as a function of time from images acquired before and after photobleaching. For further analysis, we normalize the fluorescence intensities of ROIs using the double normalization method⁷⁵. Double normalization corrects for photobleaching during the post-bleach imaging, and normalizes recovery fluorescence with a pre-bleach signal. Double-normalized intensity (I) for recovery signal can be calculated by using the following formula.

$$I = \frac{F}{F_0} \times \frac{C_0}{C}$$

where F and C are the fluorescence-integrated densities of ROIF and ROIC, respectively, for post-bleach imaging, and F_0 and C_0 correspond to pre-bleach imaging. The mobile fraction mf represents the fraction of molecules that are free to diffuse. It is estimated by using the first timepoint after bleaching (I_0) and the median of the last 20 timepoints (I_t) in the following expression:

$$mf = \frac{I_t - I_0}{1 - I_0}$$

FLIP model. FLIP is used to assess influx and efflux rates of the different constructs. FLIP experiments involve continual bleaching of an ROI and tracking signal loss from different regions. Quantification of these curves yields the transport dynamics between nucleus and cytoplasm. We set up experiments and analysis motivated from ref.²⁰ for determining the rates of nuclear influx and efflux.

To model the FLIP data, we developed a system of ordinary differential equations (ODEs) describing the change in protein concentration between two compartments, that is, the nucleus and the cytoplasm. These two compartments are linked with boundary fluxes going in (Q_i) and out (Q_e) of the nucleus (Supplementary Fig. 1).

We assume that the proteins remain in unbound and mobile state in each compartment. During steady state, cells maintain a constant ratio (α) of protein concentration between nucleus (n) and cytoplasm (c), and the flux between both compartments is equal.

$$\alpha = \frac{n}{c}$$

$$Q_e = Q_i$$

During photobleaching, the transport equations for the number of unbleached molecules in nucleus (N) and cytoplasm (C) can be described as follows, where (Q_b) is the number of molecules being bleached per unit time.

$$\frac{dN}{dt} = -Q_e + Q_i$$

$$\frac{dC}{dt} = +Q_e - Q_i - Q_b$$

The fluxes are proportional to the concentration of the compartment, times a rate coefficient. Here, k_e' and k_i' are efflux and influx rate coefficients, respectively, and η' is the bleaching rate:

$$Q_e = k_e' n \quad Q_i = k_i' c \quad Q_b = \eta' c$$

Because these rates (in units of volume per unit time) will depend on the size of the compartment, we define normalized rates as $k_e = k_e'/V_n$, $k_i = k_i'/V_n$, $\eta = \eta'/V_n$, where V_n is the volume of the nucleus. Note that we normalize both k_e and k_i by the same volume (that of the nucleus, V_n) so that the values remain comparable, and that equal k_e and k_i correspond to equal concentrations in nucleus and cytoplasm. Thus:

$$Q_e = V_n k_e n \quad Q_i = V_n k_i c \quad Q_b = V_n \eta c$$

This enables us to rewrite transport equations in terms of concentration. During bleaching,

$$V_n \frac{dn}{dt} = -V_n k_e n + V_n k_i c$$

$$V_n \frac{dc}{dt} = +V_n k_e n - V_n k_i c - V_n \eta c$$

Where V_c is cytoplasm volume. During steady state,

$$V_n k_e n = V_n k_i c$$

$$k_e \frac{n}{c} = k_i$$

$$k_e = \frac{k_i}{\alpha}$$

One can further simplify these by using ratio of nuclear volume to cytoplasm volume $\beta = \frac{V_n}{V_c}$

$$\frac{dn}{dt} = -k_e n + k_i c$$

$$\frac{1}{\beta} \frac{dc}{dt} = +k_e n - k_i c - \eta c$$

By substituting k_i , we get following equations to solve ultimately:

$$\frac{dn}{dt} = -(\mathbf{k}_e) n + (\mathbf{k}_e \alpha) c \quad (1)$$

$$\frac{dc}{dt} = +(\beta \mathbf{k}_e) n - (\beta \mathbf{k}_e \alpha + \beta \eta) c \quad (2)$$

We then solve these equations numerically using MATLAB function ode15s, and fit them to the experimental data to get influx/efflux rates and bleaching rates. Variables in bold are the unknowns to be fitted with fminsearch function in MATLAB (R2020b).

FLIP imaging and analysis. For quantification of FLIP experiments, we followed the fluorescence intensities of three different regions, segmented manually: nucleus, cell and background. Image acquisition was done with a Zeiss LSM880 inverted confocal microscope objective and using Zeiss ZEN2.3 SP1 FP3 (black, version 14.0.24.201), using a 63×1.46 NA oil immersion objective and a 488 nm wavelength argon laser. We used a bleaching ROI of 17×17 ($\sim 12.9 \mu\text{m}^2$) pixels. Ten baseline images were acquired every 3 s before photobleaching. Then, every 3 s (during a total of 120 s) the ROI was photobleached, and an image of 512×512 pixels was acquired. The power of the laser used to bleach was adjusted to result in the same bleaching rate η . Owing to differences in cell morphology, this corresponded to 60% power for cells on 1.5 kPa substrates, and 100% power for cells on 30 kPa substrates. This difference occurred because cells were more rounded on soft gels and therefore thicker in the z axis, leading to a taller column of cytoplasm affected by photobleaching. Cells with bleaching rates above 0.12 were discarded. We note that differences in obtained rates between 1.5 kPa and 30 kPa substrates were reproduced when comparing cells at 30 kPa with/without DN-KASH overexpression, where cell morphologies and bleaching laser power was not altered. In the mathematical model, the transport between nucleus and cytoplasm is modelled as transport between two compartments, where the cytoplasm is continuously bleached. We assume that the concentration of protein is uniform in each compartment and that during steady state (before photobleaching) the ratio (α) between nucleus and cytoplasm protein concentration is constant. The ROIs identified for nucleus and cytoplasm were narrow rings around the nucleus, either inside or outside of the nucleus. The average fluorescence intensity of these regions was used as a proxy for nuclear concentration (n) and cytoplasmic concentration (c). The intensities were corrected for background noise, and normalized by the total integrated cell intensity. Experimental data for n and c was used to solve Eqs. 1 and 2, as explained above. The ratio of concentrations at steady state (α) was taken as n/c at the initial timepoint (before photobleaching). To calculate the ratio of N/C volume (β), we first took confocal stacks of cells with a nuclear fluorescent label (DAPI) and whole-cell fluorescent label (GFP), seeded on both 1.5 kPa and 30 kPa gels. In those cells, we noted an excellent correlation between the N/C ratio volume ratio β , and the N/C area ratio, calculated with nuclear and cytosolic areas at a representative central slice of the cell (Extended Data Fig. 1). Thus, in FLIP experiments we measured area ratios from images, and converted this to volume ratios using the experimental correlation.

To solve for unknown variables, we used a curve fitting technique with a weighted least-square method. The experimental data for concentrations (n and c) is fitted to a solution of the ODEs (n_f , c_f). The objective function f is then formulated as the sum of squares of residuals of model and experimental data as:

$$f = \sum_t w_n (n - n_f)^2 + w_c (c - c_f)^2$$

where w_n and w_c are used to weigh the function by time and compartment concentration to avoid bias in the fitting:

$$w_n = \frac{1}{(t + \epsilon) \sum_t n} \quad w_c = \frac{1}{(t + \epsilon) \sum_t c}$$

Here, w_n , w_c , n , c and n_f and c_f are all a function of time t and ϵ is an arbitrary scalar constant (set to 10) used simply to prevent the denominator of w_n and w_c from reaching zero. We use the fminsearch function of MATLAB to minimize f as a function of ODE parameters k_e and η (Eqs. 1 and 2). For each iteration, n_f and c_f are calculated as a function of k_e and η using the MATLAB ode15s solver. We note that resulting fitted rates showed more variability for conditions with fast rates (corresponding to small MW constructs) than conditions with slow rates (Fig. 2e,f). This is probably caused by a higher experimental error in measuring fast rates: in cells with faster rates, photobleaching occurs faster, and therefore the important part of the fluorescence intensity curves is compressed in a shorter interval (fewer frames). This makes the subsequent fitting more susceptible to noise.

Statistical and reproducibility. Statistical analysis was performed with GraphPad Prism 9.0.0. When testing data with two-way analysis of variance (ANOVA), we transformed the data ($y = \log_{10}y$), which showed smaller residuals, and therefore better statistical power, when transformed.

All micrograph images shown in the figures are representative examples of results from three different experiments.

Reporting summary. Further information on research design is available in the Nature Research Reporting Summary linked to this article.

Data availability

Source data are provided with this paper. All other data supporting the findings of this study are available from the corresponding author on reasonable request.

Code availability

All codes generated during the current study are available from the corresponding authors on reasonable request. The kinetic mathematical model of transport is available at https://github.com/ravehlab/npctransport_kinetic.

References

67. Roca-Cusachs, P. et al. Integrin-dependent force transmission to the extracellular matrix by α -actinin triggers adhesion maturation. *Proc. Natl Acad. Sci. USA* **110**, E1361–E1370 (2013).
68. Liu, H. & Naismith, J. H. An efficient one-step site-directed deletion, insertion, single and multiple-site plasmid mutagenesis protocol. *BMC Biotechnol.* **8**, 91 (2008).
69. Zhang, Q. et al. Nesprins: a novel family of spectrin-repeat-containing proteins that localize to the nuclear membrane in multiple tissues. *J. Cell Sci.* **114**, 4485–4498 (2001).
70. Kazgan, N., Williams, T., Forsberg, L. J. & Brenman, J. E. Identification of a nuclear export signal in the catalytic subunit of AMP-activated protein kinase. *Mol. Biol. Cell* **21**, 3433–3442 (2010).
71. Yang, J. et al. Twist, a master regulator of morphogenesis, plays an essential role in tumor metastasis. *Cell* **117**, 927–939 (2004).
72. Oria, R. et al. Force loading explains spatial sensing of ligands by cells. *Nature* **552**, 219–224 (2017).
73. Lakins, J. N., Chin, A. R. & Weaver, V. M. Exploring the link between human embryonic stem cell organization and fate using tension-calibrated extracellular matrix functionalized polyacrylamide gels. *Methods Mol. Biol.* **916**, 317–350 (2012).
74. Elosegui-Artola, A. et al. Rigidity sensing and adaptation through regulation of integrin types. *Nat. Mater.* **13**, 631–637 (2014).
75. Rapsomaniki, M. A. et al. EasyFRAP: an interactive, easy-to-use tool for qualitative and quantitative analysis of FRAP data. *Bioinformatics* **28**, 1800–1801 (2012).

Acknowledgements

We thank S. Usieto for technical support, and G. Ceada, S. Conti, M. González, S. Garcia-Manyes, M. Rout and the members of the Roca-Cusachs and Trepab lab for useful feedback and discussions. We acknowledge funding from the Spanish Ministry of Science and Innovation (PGC2018-099645-B-I00 to X.T., BFU2016-79916-P and PID2019-110298GB-I00 to P.R.-C.), the European Commission (H2020-FETPROACT-01-2016-731957 to X.T. and P.R.-C.), the European Research Council (Adv-883739 to X.T.), the Generalitat de Catalunya (2017-SGR-1602 to X.T. and P.R.-C.), The prize ‘ICREA Academia’ for excellence in research to P.R.-C., Fundació la Marató de TV3 (201936-30-31 to P.R.-C.) and ‘la Caixa’ Foundation (grant LCF/PR/HR20/52400004 to X.T. and P.R.-C. and fellowships LCF/BQ/DR19/11740009 to I.G.-M. and LCF/BQ/DR19/11740009 to M.M.J.). A.E.M.B. is recipient of a Sir Henry Wellcome fellowship (210887/Z/18/Z). The Institute for Bioengineering of Catalonia (IBEC) is a recipient of a Severo Ochoa Award of Excellence from MICIN.

Author contributions

I.A. and P.R.-C. conceived the study; I.A. and P.R.-C. designed the experiments; I.A., I.G.-M., M.M.J., A.E.M.B. and A.E.-A. performed the experiments; I.A., I.G.-M., N.R.C., J.E.A., L.R., X.T., B.R. and P.R.-C. analysed the experiments; I.G.-M. designed and cloned all constructs, N.R.C. implemented the FLIP analysis software, K.C. and B.R. implemented the kinetic model of transport, and I.A., I.G.-M. and P.R.-C. wrote the manuscript. All authors commented on the manuscript and contributed to it.

Competing interests

The authors declare no competing interests.

Additional information

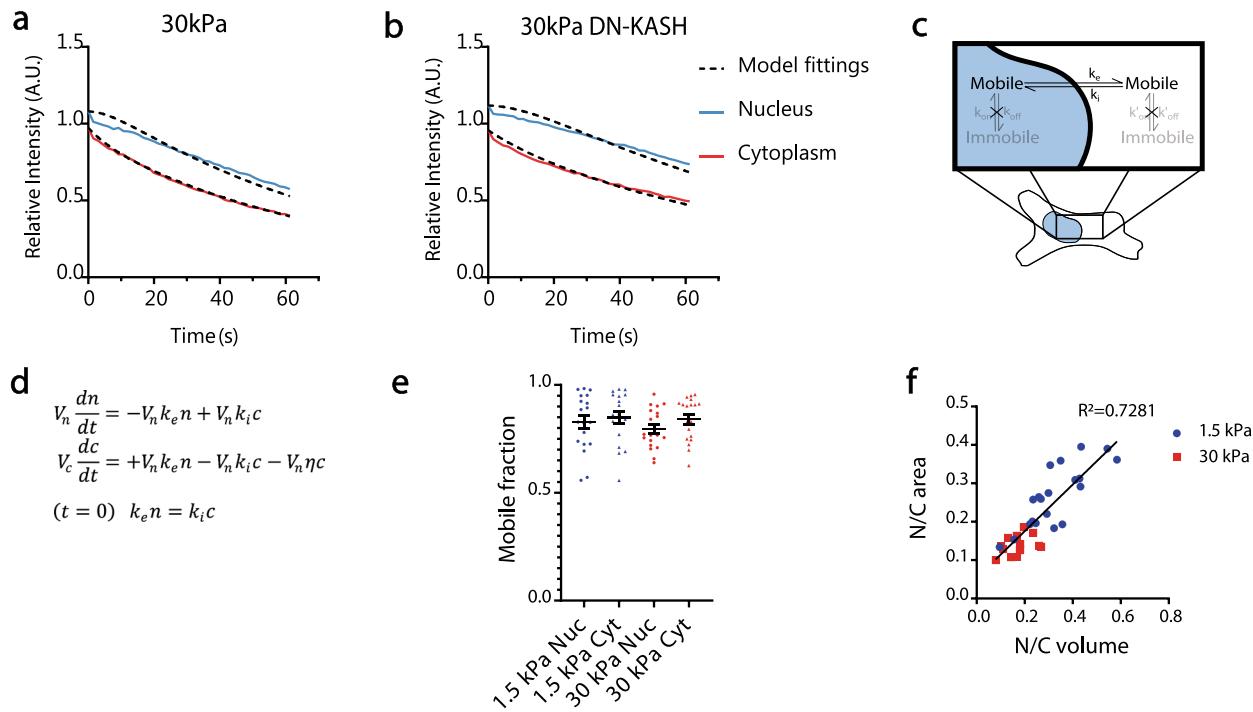
Extended data is available for this paper at <https://doi.org/10.1038/s41556-022-00927-7>.

Supplementary information The online version contains supplementary material available at <https://doi.org/10.1038/s41556-022-00927-7>.

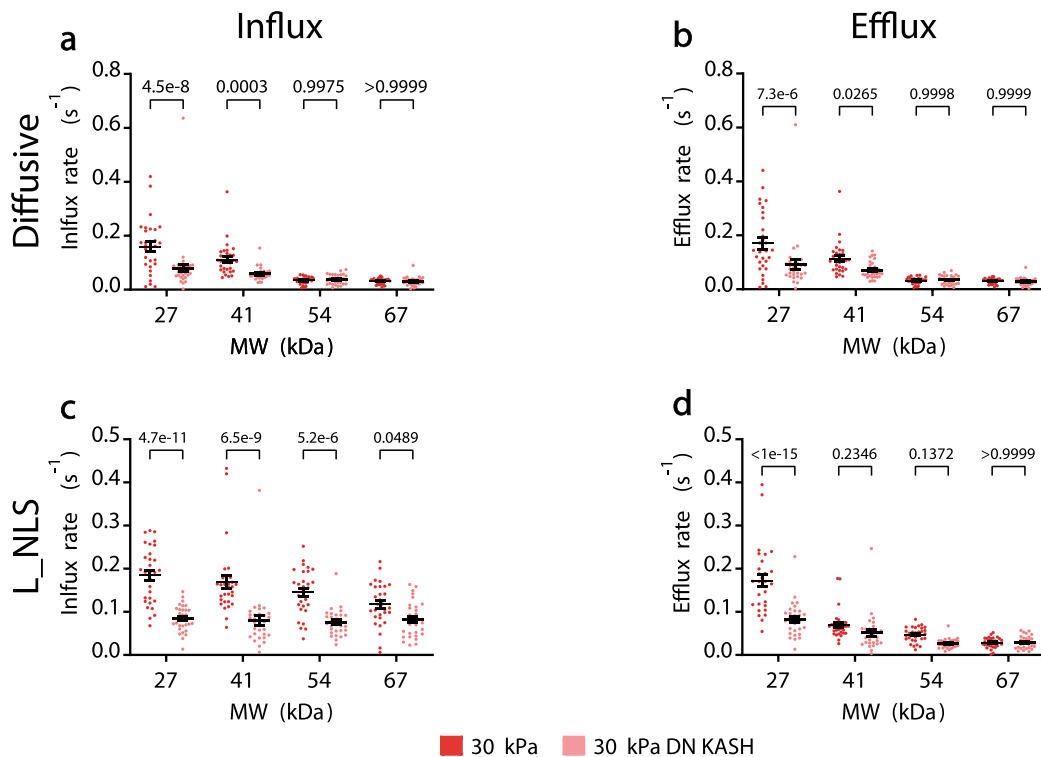
Correspondence and requests for materials should be addressed to Ion Andreu or Pere Roca-Cusachs.

Peer review information *Nature Cell Biology* thanks Dennis Discher, Michael Elbaum, André Hoelz and the other, anonymous reviewer(s) for their contribution to the peer review of this work. Peer reviewer reports are available.

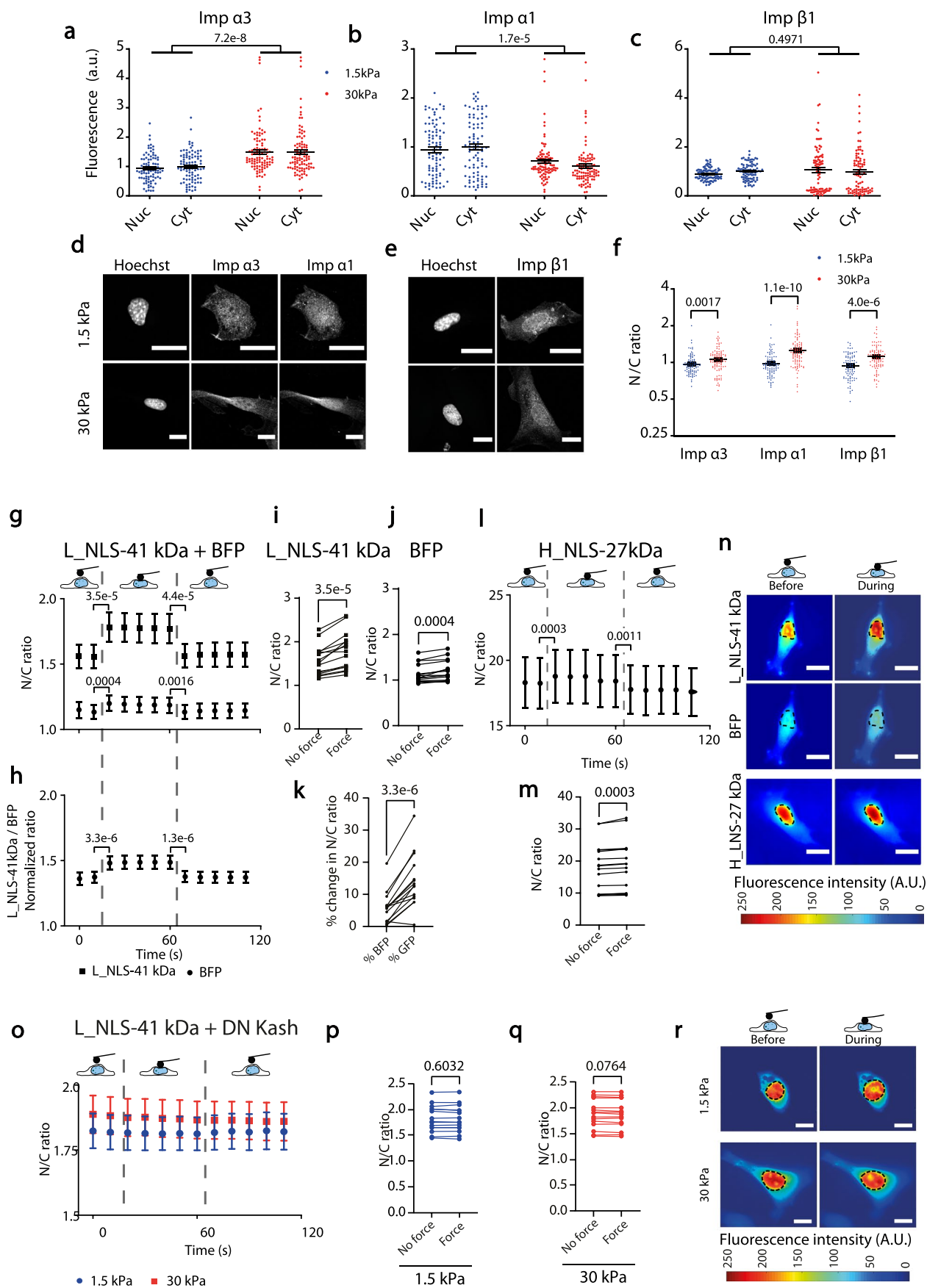
Reprints and permissions information is available at www.nature.com/reprints.



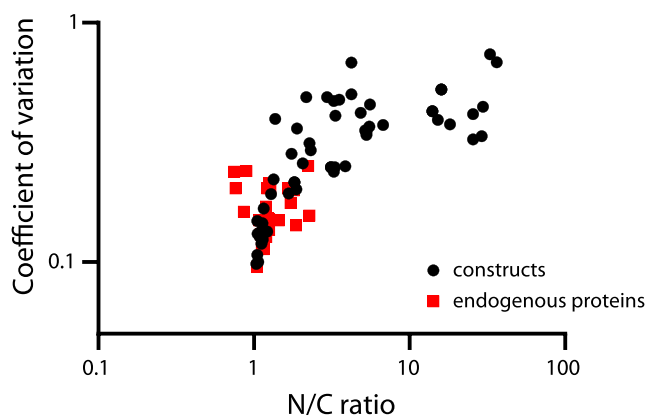
Extended Data Fig. 1 | Fluorescence Loss In Photobleaching (FLIP) technique. **a, b**) Examples of curves showing fluorescence intensity as a function of time in the nucleus and cytoplasm in FLIP experiments on two example cells transfected with the diffusive 41 kDa construct and seeded on a) 30 kPa in control condition and b) 30kPa with DN-KASH overexpression. Data represent the mean fluorescence intensity of the compartments (nucleus/cytoplasm), normalized with the mean of the whole cell before the beginning of photobleaching, and corrected for background signal. Each curve depicts a representative experiment of one cell each. **c, d)** Cartoon and equations describing the model used for fitting curves as in A,B, and calculating influx and efflux rates. The model considers the molecules to freely diffuse inside the nuclear and cytoplasmic compartments (see methods). **e**) Mobile fraction of the L-NLS 41 kDa construct in the nucleus (Nuc) and cytoplasm (Cyt) of cells seeded on 1.5/30 kPa gels. N=19 cells from 3 independent experiments, lines show mean \pm SEM **f**) For cells seeded on 1.5 and 30 kPa gels, correlation between nuclear to cytosolic ratios of volume, and of areas as measured in confocal slices used for FLIP measurements; regression equation $y=0.6075x+0.05375$. N=20 (1.5kPa) and N=14 (30kPa) cells from 2 independent experiments. Black line shows the linear regression. Source numerical data are available in source data.



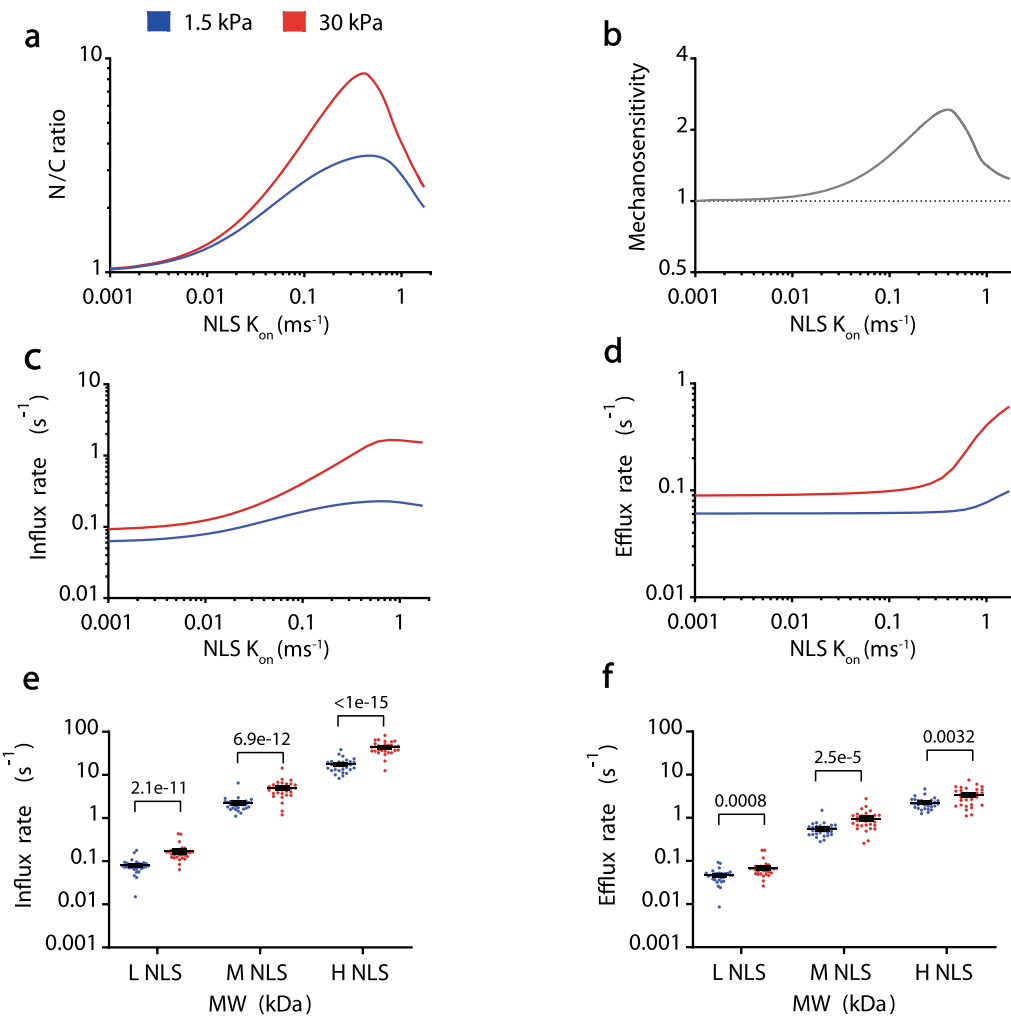
Extended Data Fig. 2 | Blocking nuclear to cytoskeletal force transmission with DN-KASH recapitulates the effects of substrate stiffness on transport rates. **a, b)** Influx and efflux rates of diffusive constructs for cells seeded on 30 kPa gels, with or without DN-KASH overexpression. In a, both MW ($p < 1e-15$) and DN KASH ($p = 1e-6$) effects tested significant. In b, both MW ($p < 1e-15$) and DN KASH ($p = 0,0002$) effects tested significant. **c, d)** Influx and efflux rates of constructs containing L-NLS for cells seeded on 30 kPa gels, with or without DN-KASH overexpression. In c, both MW ($p = 0,0025$) and DN KASH ($p < 1e-15$) effects tested significant. In d, both MW ($p < 1e-15$) and DN KASH ($p = 3.4e-10$) effects tested significant. In all panels, $N=30$ cells from 3 independent experiments. Two-way ANOVA, Šídák's multiple comparisons test was used to obtain p-values between conditions. Data are mean \pm SEM. Source numerical data are available in source data.



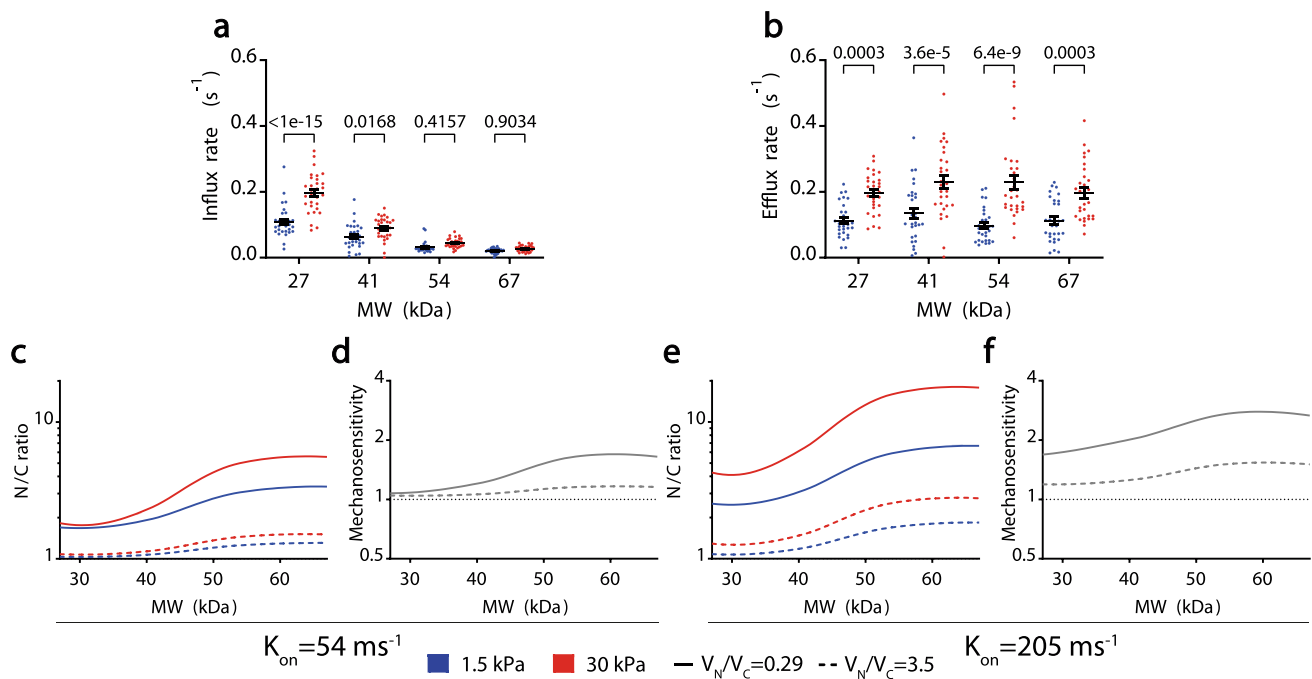
Extended Data Fig. 3 | Control experiments on importins and AFM. **a-c)** Average fluorescence intensities of nuclear and cytoplasmic areas of cells seeded on substrates of 1.5 or 30 kPa stiffness and immunostained for importin $\alpha 3$ (imp $\alpha 3$) importin $\alpha 1$ (imp $\alpha 1$), and importin $\beta 1$ (imp $\beta 1$). N=90 cells from 3 independent experiments. The effect of substrate stiffness tested significant for importin $\alpha 3$ ($p=7.2e-8$) and importin $\alpha 1$ ($p=1.7e-5$), but not for importin $\beta 1$ ($p=0.4971$). p-values from Two-way ANOVA **d-e)** Corresponding example images showing the nucleus (Hoechst) and the distribution of the different importins. **f)** Corresponding quantification of nuclear to cytoplasmic ratio of importin localization. N=91,98, 91, 98, 90, 90 cells (from left to right) from 3 independent experiments. p-values from independent two-tailed Mann-Whitney tests. **g)** N/C ratios of L_NLS-41 kDa or BFP constructs in cells seeded on 1.5 kPa gels before, during, and after nuclear deformation with AFM. **h)** L_NLS-41 kDa ratios normalized by BFP ratios, from panel g) paired measures. **i,j)** from g, corresponding paired dot plots of the time points right before and after force application. **k)** from g, corresponding % change in N/C ratios right after force application for both constructs. In g,h,i,j,k N=15 cells from 3 independent experiments, p-values were calculated with a two-tailed paired t-test. **l)** N/C ratios of H_NLS-27 kDa construct in cells seeded on 1.5 kPa gels before, during, and after nuclear deformation with AFM. **m)** from l, corresponding paired dot plots of the time points right before and after force application. In l, m, N=15 cells from 3 independent experiments. p-values were calculated with a two-tailed paired t-test. **n)** Corresponding images of constructs before and during force application, dotted line marks nucleus outline. **o)** N/C ratios of the L_NLS-41 kDa construct in cells co-transfected with DN-KASH and seeded on 1.5 or 30 kPa gels before, during, and after nuclear deformation with AFM. Data are mean \pm SEM. **p,q)** from o, corresponding paired dot plots of the time points right before and after force application. In o,p,q, N=15 cells from 3 independent experiments. p-values were calculated with a two-tailed paired t-test, traces of all cells are shown in Extended Data Fig. 8. **r)** Corresponding images of constructs before and during force application, dotted line marks nucleus outline. Scale bars, 20 μ m. Note: in AFM experiments, non-mechanosensitive constructs (BFP and H_NLS) still show a small increase with force, likely due to lensing effects caused by changes in cell shape during indentation. This increase (~6% for BFP, ~2% for H_NLS) is much smaller than that of the mechanosensitive construct (L_NLS 41kDa, ~14%), see panel k. Panel h in fact shows the response of the L_NLS construct after factoring out the response of BFP. Data are mean \pm SEM in all panels. Source numerical data are available in source data.



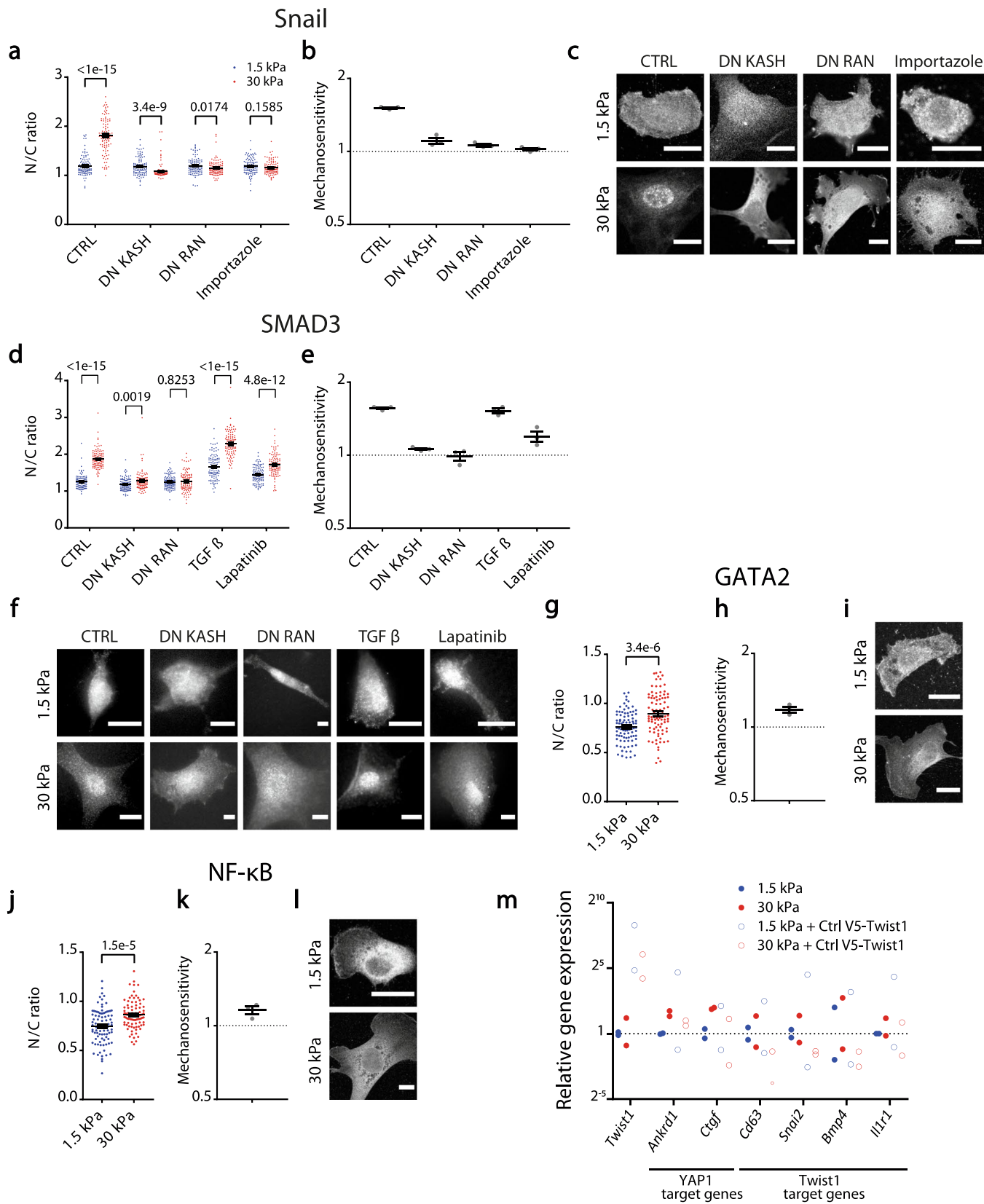
Extended Data Fig. 4 | Noise levels in N/C ratio measurements. Relationship between mean N/C ratio as reported in figures, and corresponding coefficient of variation (standard deviation divided by the mean). The different points show all different constructs and conditions reported in the manuscript. Black dots indicate values of overexpressed engineered constructs, red squares indicate values of stained endogenous proteins. Source numerical data are available in source data.



Extended Data Fig. 5 | Effect of the affinity of the NLS signal in influx and efflux rates. (a-d) Model predictions for N/C ratios (a), mechanosensitivities (b), influx rates (c) and efflux rates (d) for 41 kDa constructs as a function of NLS affinity (modelled by the binding rate k_{on} between the NLS and importin α). (e,f) Experimental Influx and efflux rates of 41 kDa constructs containing NLS signals of different affinity for importin β . In both cases (e,f), NLS strength and substrate stiffness effects tested significant (respectively: e) $p < 1 \times 10^{-15}$, f) $p < 1 \times 10^{-15}$, $p = 2.4 \times 10^{-10}$). N = 30 cells from 3 independent experiments. p-values from Two-way ANOVA. Data are mean \pm SEM. Source numerical data are available in source data.

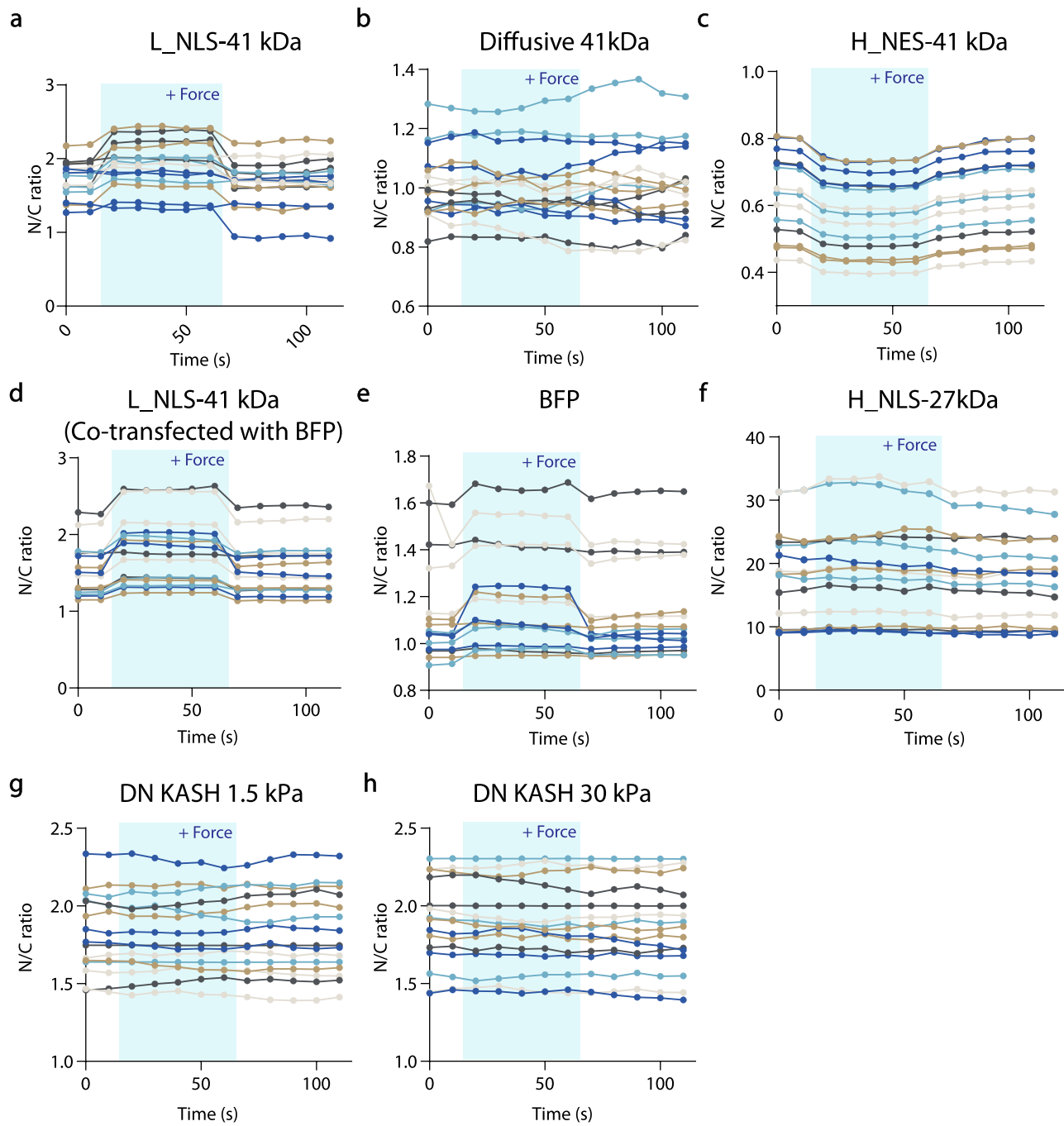


Extended Data Fig. 6 | Further experiments and modelling results regarding NES constructs. For M_NES constructs, influx rates (mediated by passive transport) and efflux rates (mediated by facilitated transport) as a function of molecular weight. $N=30$ cells from 3 independent experiments. Substrate stiffness effects tested significant in both cases (a) $p=5.1e-13$; (b) $p<1e-15$; MW only tested significant for influx, a) $p<1e-15$; b) $p=0.2138$. Two-way ANOVA, Šídák's multiple comparisons test was used to obtain p-values between conditions. Data presented as mean \pm SEM. **c, d** Model predictions of N/C ratios (c) and mechanosensitivities (d) for an NLS with a binding rate k_{on} of 54 ms^{-1} as a function of MW. Data are shown for experimentally measured N/C volume ratios (0.29) and for inverted volume ratios (3.5). **e, f** Same predictions as in c,d for an NLS with a binding rate k_{on} of 205 ms^{-1} . Note that these predictions simply evaluate the role of N/C volumes on import, they do not explicitly model the export cycle (and hence mechanosensitivities are above and not below 1). Source numerical data are available in source data.



Extended Data Fig. 7 | See next page for caption.

Extended Data Fig. 7 | Mechanosensitivity of transcriptional Regulators. **a-c**) For Snail stainings at different conditions, quantifications of N/C ratios on 1.5/30 kPa substrates (a, N=100 cells from 3 independent repeats), corresponding mechanosensitivities for the 3 different repeats (b), and representative images (c). **d-f**) For SMAD3 stainings at different conditions, quantifications of N/C ratios on 1.5/30 kPa substrates (d, N=100 cells from 3 different repeats), corresponding mechanosensitivities for the 3 different repeats (e), and representative images (f). **g-i**) For GATA2 stainings at different conditions, quantifications of N/C ratios on 1.5/30 kPa substrates (g, N=90 cells from 3 independent repeats), Corresponding mechanosensitivities for the 3 different repeats (h), and representative images (i). **j-l**) For NF- κ B stainings at different conditions, quantifications of N/C ratios on 1.5/30 kPa substrates, (j, N=90 cells from 3 independent repeats), corresponding mechanosensitivities for the 3 different repeats (k), and representative images (l). For a-l, data are presented as mean \pm SEM, scale bars correspond to 20 μ m, and p-values from corrected multiple two-tailed Mann-Whitney (a,d) and two-tailed Mann-Whitney (g,j) tests. **m**) Relative gene expression of different genes as assessed with qPCR. Conditions are cells seeded on 1.5 or 30 kPa substrates, overexpressing or not a WT twist1 construct (Ctrl V5-twist1). Gene expression is shown relative to the 1.5 kPa condition without overexpression. n=2 independent experimental repeats. Source numerical data are available in source data.



Extended Data Fig. 8 | Cell-by-cell fluorescence curves of all AFM experiments. Plots showing the evolution with time of N/C ratios before, during and after force application to the cell nucleus for all cells measured. **a, b)** AFM experiments reported in Fig. 3, **c)** Fig. 5, and **d-h)** Extended Data Fig. 3. Source numerical data are available in source data.

Reporting Summary

Nature Portfolio wishes to improve the reproducibility of the work that we publish. This form provides structure for consistency and transparency in reporting. For further information on Nature Portfolio policies, see our [Editorial Policies](#) and the [Editorial Policy Checklist](#).

Statistics

For all statistical analyses, confirm that the following items are present in the figure legend, table legend, main text, or Methods section.

n/a Confirmed

- The exact sample size (n) for each experimental group/condition, given as a discrete number and unit of measurement
- A statement on whether measurements were taken from distinct samples or whether the same sample was measured repeatedly
- The statistical test(s) used AND whether they are one- or two-sided
Only common tests should be described solely by name; describe more complex techniques in the Methods section.
- A description of all covariates tested
- A description of any assumptions or corrections, such as tests of normality and adjustment for multiple comparisons
- A full description of the statistical parameters including central tendency (e.g. means) or other basic estimates (e.g. regression coefficient) AND variation (e.g. standard deviation) or associated estimates of uncertainty (e.g. confidence intervals)
- For null hypothesis testing, the test statistic (e.g. F , t , r) with confidence intervals, effect sizes, degrees of freedom and P value noted
Give P values as exact values whenever suitable.
- For Bayesian analysis, information on the choice of priors and Markov chain Monte Carlo settings
- For hierarchical and complex designs, identification of the appropriate level for tests and full reporting of outcomes
- Estimates of effect sizes (e.g. Cohen's d , Pearson's r), indicating how they were calculated

Our web collection on [statistics for biologists](#) contains articles on many of the points above.

Software and code

Policy information about [availability of computer code](#)

Data collection	Microscopy images were acquired by using Zeiss ZEN2.3 SP1 FP3 (black, version 14.0.24.201) or Micromanager (version 1.4.22). AFM data was acquired using the JPK software (JPK Data Processing Version 6.1.79).
Data analysis	Immunostaining images were analyzed with ImageJ (version 1.53e). Data statistical tests were performed with Graphpad PRISM (version 9). FLIP and FRAP data were analyzed with custom matlab scripts (Matlab R2020b). The kinetic mathematical model of transport was implemented in Python (version 3.6). The source code and the run parameters can be found in https://github.com/ravehlab/npctransport_kinetic .

For manuscripts utilizing custom algorithms or software that are central to the research but not yet described in published literature, software must be made available to editors and reviewers. We strongly encourage code deposition in a community repository (e.g. GitHub). See the Nature Portfolio [guidelines for submitting code & software](#) for further information.

Data

Policy information about [availability of data](#)

All manuscripts must include a [data availability statement](#). This statement should provide the following information, where applicable:

- Accession codes, unique identifiers, or web links for publicly available datasets
- A description of any restrictions on data availability
- For clinical datasets or third party data, please ensure that the statement adheres to our [policy](#)

All data generated or analysed during this study are included in a supplementary source data file.

Field-specific reporting

Please select the one below that is the best fit for your research. If you are not sure, read the appropriate sections before making your selection.

Life sciences

Behavioural & social sciences

Ecological, evolutionary & environmental sciences

For a reference copy of the document with all sections, see nature.com/documents/nr-reporting-summary-flat.pdf

Life sciences study design

All studies must disclose on these points even when the disclosure is negative.

Sample size	No statistical methods were used to determine sample size before execution of the experiments. Sample sizes for number of cells were determined based on previous experience by our group and others on similar experiments (Elosegui-Artola et al., Cell 171(6):1397-1410, 2017).
Data exclusions	No data was excluded from the analyses.
Replication	All experimental findings were replicated independently at least three times, except data in extended data fig. 1f and data in extended data fig. 7m, which were replicated independently two times.
Randomization	Cells were measured at random within each condition. Sample allocation was also random (all cells came from the same culture before the indicated treatments, and there was no control over which cell was submitted to each treatment).
Blinding	No blinding was carried out as all measurements reported are quantitative and cannot be biased by subjective perception.

Reporting for specific materials, systems and methods

We require information from authors about some types of materials, experimental systems and methods used in many studies. Here, indicate whether each material, system or method listed is relevant to your study. If you are not sure if a list item applies to your research, read the appropriate section before selecting a response.

Materials & experimental systems

n/a	Involved in the study
<input type="checkbox"/>	<input checked="" type="checkbox"/> Antibodies
<input type="checkbox"/>	<input checked="" type="checkbox"/> Eukaryotic cell lines
<input checked="" type="checkbox"/>	<input type="checkbox"/> Palaeontology and archaeology
<input checked="" type="checkbox"/>	<input type="checkbox"/> Animals and other organisms
<input checked="" type="checkbox"/>	<input type="checkbox"/> Human research participants
<input checked="" type="checkbox"/>	<input type="checkbox"/> Clinical data
<input checked="" type="checkbox"/>	<input type="checkbox"/> Dual use research of concern

Methods

n/a	Involved in the study
<input type="checkbox"/>	<input checked="" type="checkbox"/> ChIP-seq
<input checked="" type="checkbox"/>	<input type="checkbox"/> Flow cytometry
<input checked="" type="checkbox"/>	<input type="checkbox"/> MRI-based neuroimaging

Antibodies

Antibodies used

For primary antibodies, we used Anti Twist antibody (Twist2C1A, Santa cruz, sc-81417, RRID:AB_1130910) 1:200, Mouse monoclonal antibody to SNAIL + SLUG - N-terminal (clone number: CL3700; abcam, ab224731) 1:200, rabbit polyclonal anti SMAD3 (Cell Signaling, 9513, RRID:AB_2286450) 1:40, Rabbit polyclonal antibody to GATA2 (Abcam, ab153820) 1:200, rabbit polyclonal Anti-NF-kB p65 antibody (abcam, ab16502, RRID:AB_443394) 1:200, KPNA4 / Importin alpha 3 (NBP1-31260 Novus Biologicals, RRID:AB_2133841) 1:200, KPNA2 / Importin alpha 1 (MAB6207 Bio-techne, Clone number: 682239) 1:200, KPNB1 / Importin Beta 1 (ab2811 Abcam, RRID:AB_2133989) 1:200. The secondary antibodies used were Alexa Fluor 488 anti-mouse (A-11029; Thermo Fischer Scientific, RRID:AB_2534088) and Alexa Fluor 555 anti-rabbit (A-21429; Thermo Fischer Scientific, RRID:AB_2535850) diluted 1:200.

Validation

Anti Twist antibody was validated for detecting murine Twist via WB, IP, IF and FCM. Mouse monoclonal antibody to SNAIL + SLUG was validated for IHC-P, ICC/IF in humans and predicted to work with mouse by the provider and validated via independent research articles. Rabbit polyclonal anti SMAD3 was validated for use in mice in WB, IP, IHC, ChIP, IF, FC. Rabbit polyclonal antibody to GATA2 was validated for use in human in WB, ICC/IF (97.37% identity between mouse and human immunogenic regions). Rabbit polyclonal Anti-NF-kB p65 antibody was validated for use in mouse in ICC/IF, IHC-P, WB, IP. KPNA4 / Importin alpha 3 was validated for use in mouse in WB, ICC/IF, IHC, IHC-P KPNA2 / Importin alpha 1 was validated for use in human in WB, ICC/IF and in mouse by independent research articles. KPNB1 / Importin Beta 1 was validated for use in mouse in FC, IP, WB, ICC/IF.

Eukaryotic cell lines

Policy information about [cell lines](#)

Cell line source(s)

Male mouse embryonic fibroblasts were described previously (Roca-Cusachs et al., 2013) and created at Department of Pharmacology, Kaplan Cancer Center, New York University School of Medicine, 550 First Avenue, New York, New York 10016, USA.

Authentication

Cell lines used were not authenticated.

Mycoplasma contamination

Cell cultures were routinely checked for mycoplasma. Cell lines tested negative for mycoplasma contamination.

Commonly misidentified lines
(See [ICLAC](#) register)

No commonly misidentified lines were used.